

JOYS: JWST MIRI/MRS spectra of the inner 500 au region of the L1527 IRS bipolar outflow

R. Devaraj,¹, E. F. van Dishoeck², T. P. Ray¹, Ł. Tychoniec², A. Caratti o Garatti³, L. Francis², C. Gieser⁴, M. L. van Gelder², J. J. Tobin⁵, H. Beuther⁴, P. J. Kavanagh⁶, K. Justtanont⁷, W. B. Drechsler⁸, M. G. Navarro⁹ and G. Perotti⁴

¹ School of Cosmic Physics, Dublin Institute for Advanced Studies, 31 Fitzwilliam Place, Dublin 2, Ireland

² Leiden Observatory, Leiden University, P.O. Box 9513, NL 2300 RA Leiden, The Netherlands

³ INAF-Osservatorio Astronomico di Capodimonte, Salita Moiariello 16, I-80131 Napoli, Italy

⁴ Max Planck Institute for Astronomy, Königstuhl 17, 69117 Heidelberg, Germany

⁵ National Radio Astronomy Observatory, 520 Edgemont Road, Charlottesville, VA 22903, USA

⁶ Department of Physics, Maynooth University, Maynooth, Co. Kildare, Ireland

⁷ Department of Space, Earth and Environment, Chalmers University of Technology, Onsala Space Observatory, 43992 Onsala, Sweden

⁸ Department of Astronomy, University of Virginia, Charlottesville, VA 22904, USA

⁹ INAF-Osservatorio Astronomico di Roma, Via di Frascati 33, 00078 Monte Porzio Catone, Italy

Version of January 27, 2026

ABSTRACT

Context. Outflows and jets are defining characteristics in protostellar evolution, intimately linked to accretion. Understanding their properties and origins is essential to probing the earliest phases of star formation.

Aims. This study characterizes the physical and kinematic properties within the innermost 500 au region of the L1527 bipolar outflow, a Class 0/I low-mass protostar, as part of the JWST Observations of Young protoStars (JOYS) program.

Methods. We obtain spectroscopic observations using JWST MIRI/MRS instrument across 5 – 28 μ m at 0.2 – 1.0'' spatial resolution. We identify emission lines from molecular and ionized species and analyze their spatial morphology using line integrated intensity maps. We derive gas temperature and column density through excitation diagram analysis of H₂ rotational lines and compared results with shock models.

Results. The observations reveal extended molecular hydrogen emission tracing the bipolar outflow, with the H₂ gas temperatures distributed into warm (\sim 550 K) and hot (\sim 2500 K) components, likely originating from moderate velocity *J*-type shocks and some UV irradiation. We detect forbidden atomic and ionized emission lines of [Ni II], [Ar II], [Ne II], [Ne III], [S I], and [Fe II] showing spatially extended morphology. Double peaked emission profiles were seen in [Ar II], [Ne III], and [Fe II], in the eastern region, suggesting that the high velocity component traces a fast, highly ionized jet. Radial velocity map derived from [Ne II] emission shows the eastern region to be redshifted and the western region blueshifted, contrary to earlier interpretations.

Conclusions. The analysis of the MIRI/MRS observations reveals the presence of molecular, atomic, and ionized emission lines in this low-mass protostar connected with active outflow signatures. The most striking feature discovered is the presence of a poorly collimated high velocity ionized jet, embedded within a broader wide-angle molecular outflow likely driven by a disk wind. The co-existence of these components supports a stratified outflow structure and suggest L1527 exhibits unique jet-launching characteristics atypical for its early evolutionary stage.

Key words. Stars: formation – Stars: low-mass – Stars: jets – Stars: winds, outflows – ISM: individual objects: L1527

1. Introduction

The earliest phases of protostar evolution are characterized by accretion and ejection processes, with the forming protostar deeply embedded in its natal envelope. These ejections typically show two connected but distinct observable components: 1) a highly collimated, high-velocity jet (up to several hundred km s⁻¹) whose composition varies with evolutionary stage and may include molecular, atomic, and partially ionized gas, and 2) a slower, wider-angle outflow (1–50 km s⁻¹), composed predominantly of molecular and/or atomic gas produced as the jet or a wide-angle wind entrains, shocks, and accelerates the surrounding material (Frank et al. 2014; Bally 2016; Ray & Ferreira 2021). The exact mechanism driving these outflows is debated, but the main process involves interaction of accreted matter with the stellar and/or disk magnetic field. Two main models describe

the ejection process depending on the distance from the protostar to where the gas is launched. In the X-wind models (Shu et al. 2007; Shang et al. 2007), the launch occurs very close to the protostar where stellar magnetosphere intersects with the protostellar disk. In the Disk-wind models, the winds are launched near to few au's away from the protostar along the magnetized disk surface (Blandford & Payne 1982; Shu et al. 1994). In both cases, the poloidal magnetic field plays a critical role in the initial launch and collimation of the outflow (Banerjee & Pudritz 2006, 2007). It is now understood that outflows are the main mechanism that assist in removal of angular momentum helping accretion to proceed (Ray et al. 2007; Bally 2016). Recent studies suggest that the slower and wider outflow wind influences the evolution and dispersal of protoplanetary disks (Pascucci et al. 2023). Outflows also play a vital role in limiting the star formation efficiency and shaping the initial mass function (Federrath

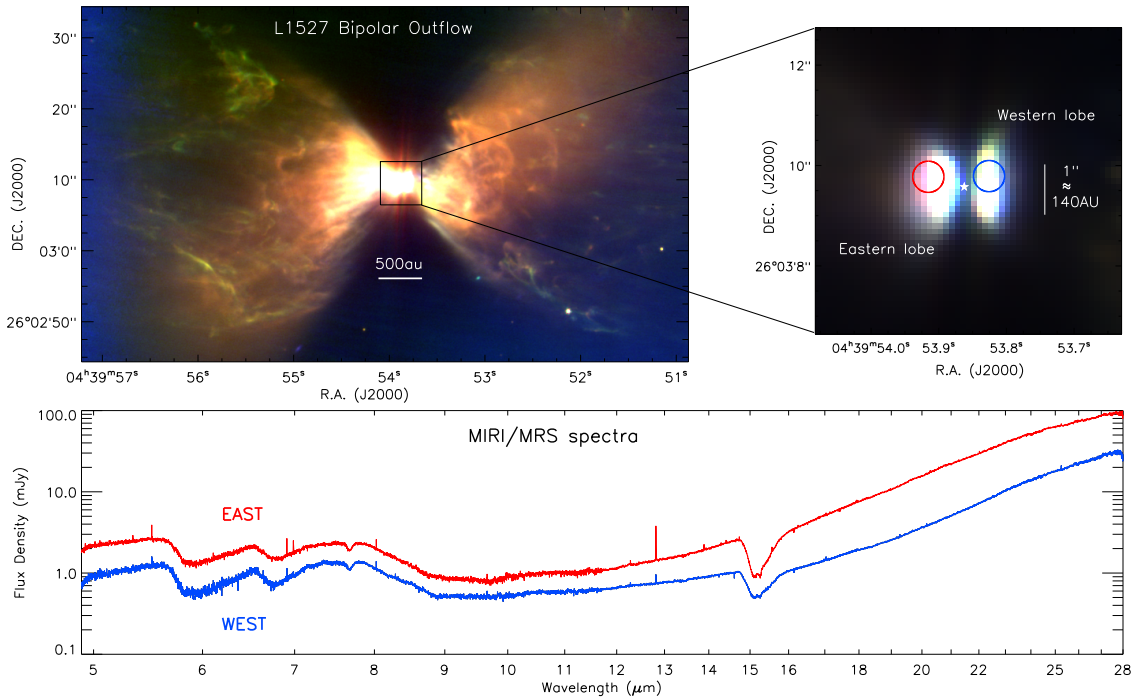


Fig. 1. Mid-infrared three-color image of the L1527 bipolar outflow, using JWST MIRI broadband imaging at $5.6\,\mu\text{m}$ (red), $7.7\,\mu\text{m}$ (green) and $12.8\,\mu\text{m}$ (blue). The region spans $1.43' \times 0.83'$, corresponding to a physical scale of $12000\,\text{au} \times 7000\,\text{au}$ at a distance of $140\,\text{pc}$. The prominent blue emission at the left edge is not physical, but an artifact of color stretch. The right panel shows a zoomed in view of the $500\,\text{au}$ central region with brightness scaled to reveal the bipolar outflow lobes. The position of the forming protostar is marked by a star symbol. Two circular apertures of $\sim 0''.3$ radius in red and blue are shown corresponding to the area where the MIRI/MRS spectra was extracted. Bottom panel shows the spectra obtained at the aperture positions across the full MIRI/MRS wavelength range ($5 - 28\,\mu\text{m}$). The red colored spectra corresponds to the eastern lobe, whereas the blue spectra corresponds to the western lobe. Flux density of both the spectra are scaled for visual offset.

2015; Guszejnov et al. 2022). They can inject energy and momentum into the surrounding medium dispersing a significant amount of the envelope (Dunham et al. 2014; Offner & Arce 2014; Zhang et al. 2016), thereby ending the infall phase of the protostar.

The outflows hold insights about the associated protostars and can reveal the nature of their origins through their morphologies, kinematics, and physical properties. Outflows can be probed using a wide array of tracers from visual to radio wavelengths. The atomic and ionized components of the outflow have been traced in the visual and near-infrared (NIR) hydrogen recombination lines (Davis et al. 2011; Nisini et al. 2024), and in many forbidden emission transitions such as [O II], [S II], [N II], [Ni II], [Ca II], and [Fe II] (Nisini et al. 2005; Pascucci et al. 2020). The molecular component of outflows have been extensively studied in the infrared and (sub)-millimeter wavelengths using the low-J pure rotational transitions of H₂ and CO (Giannini et al. 2002; Lee et al. 2002; Wu et al. 2004; Davis et al. 2010; Mottram et al. 2017; Devaraj et al. 2023). The accelerated warm and hot gas from shocks have been traced in the higher-J transitions of CO (Giannini et al. 2001; Gomez-Ruiz et al. 2012; Kristensen et al. 2017; Karska et al. 2018), and with species such as SiO (Lee 2020; Towner et al. 2023). More recently in few cases jets have been detected in radio synchrotron emission (Anglada et al. 2018; Feeney-Johansson et al. 2019). However, no tracer is complete, and because of the very high extinction, the deeply embedded regions, particularly the outflows from Class 0/I protostars have to be studied at higher angular resolutions at longer wavelengths. While (sub)-millimeter data from facilities like ALMA have allowed detailed imaging of the cold molecular material

(Arce et al. 2013; Hsieh et al. 2023), the mid-infrared (MIR) continuum and spectroscopic imaging of the warmer atomic and molecular material is essential to get a detailed characterization of the processes occurring in the outflows. The James Webb Space Telescope (JWST) (Gardner et al. 2023) with its MIR capabilities can identify and spatially resolve multiple flow components that are hidden at shorter wavelengths, thereby providing a unique window for studying the deeply embedded protostellar phase.

The object in our study is the L1527 IRS (also known as IRAS 04368+2557; hereafter L1527), a low-mass protostar located in the L1527 dark cloud (Beverly 1962) in the Taurus star-forming region. It is estimated to be at a distance of $140 \pm 1\,\text{pc}$ by the most recent studies using Gaia Data Release 2 (DR2) and very long baseline interferometry (VLBI) data (Luhman 2018; Galli et al. 2019). The protostar has been observed extensively from the near-infrared to centimeter wavelengths. The systemic velocity of the region in the local standard of rest (LSR) frame was estimated to be $V_{\text{sys,LSR}} \approx 5.9\,\text{km s}^{-1}$ (Ohashi et al. 1997; Tobin et al. 2011). The earliest evidence of outflow in L1527 was identified with (sub)-millimeter observations in CO and HCO⁺ emissions (Bontemps et al. 1996; Tamura et al. 1996; Zhou et al. 1996; Hogerheijde et al. 1998). Their outflow maps revealed a red shifted and blue shifted emission oriented in east-west direction in the plane-of-sky. A detailed picture of the outflow emission in scattered light, extending $\sim 20,000\,\text{au}$, was presented by Tobin et al. (2008, 2010) using Spitzer Space Telescope and

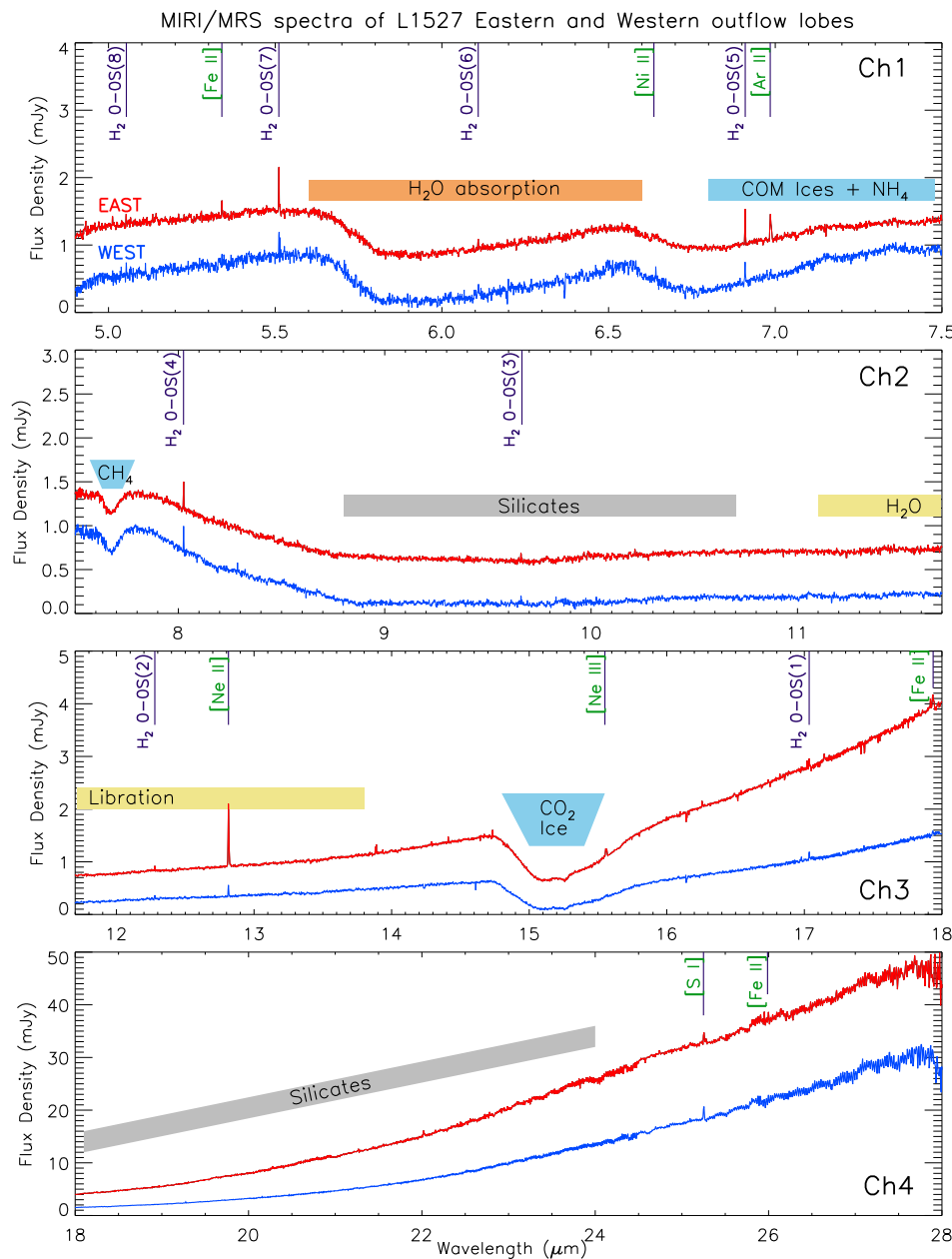


Fig. 2. Detailed MIRI/MRS spectra extracted at the aperture positions as shown in Fig. 1. The four different panels correspond to the spectra from the 4 MIRI channels. Various molecular and ionized emission lines are identified and labeled. Major solid-state absorption features from ices and silicates are indicated in wide colored bands. The red spectra is scaled with an increased offset, as to not overlap with the blue spectra.

Gemini telescope. During Cycle 1 observations, JWST released¹ a high resolution NIR broadband imaging of the outflow, revealing an intricate map of the dust layers and shocked material. Very recently, van't Hoff et al. (2023) using ALMA data, identified a blue shifted unresolved SiO emission on the western lobe indicating a tentative presence of a jet.

L1527 is often classified as a borderline Class 0/I protostar due to its low bolometric temperature (~ 40 K) and the presence of a large and massive envelope (~ 2000 au and $0.9 M_{\odot}$) (Jørgensen et al. 2007; Tobin et al. 2013; Ohashi et al. 2023). It is one of the first protostars in its earliest evolutionary stage toward which a Keplerian rotating disk was established (Tobin et al. 2012). The disk has been viewed to be edge-on and its inclination angle was estimated to be $i \approx 75 - 85^\circ$ (Tobin et al. 2008; Ohashi et al. 2023). High resolution sensitive observations of the disk have

shown it to be warped and asymmetric extending up to 100 au (Sheehan et al. 2022; van't Hoff et al. 2023). Recent analysis of the spectral energy distribution (SED) of L1527 have estimated its bolometric luminosity to be in the range of $1.6 - 2.0 L_{\odot}$ and a protostellar mass of about $0.2 - 0.4 M_{\odot}$ (Aso et al. 2013; Karska et al. 2018; Ohashi et al. 2023). Using VLA observations at 7 mm, Loinard et al. (2002) directly imaged the disk of L1527 and found an unresolved blob 25 au from the central protostar, suspecting it to be a binary companion. However, many recent high-sensitivity observations with ALMA and VLA have not been able to confirm the binarity (e.g. Nakatani et al. 2020; Sheehan et al. 2022). Although L1527 has been studied at multi-wavelengths presenting an edge-on disk, large envelope mass, and extended outflow cavities, it has not been observed to have any clear collimated high-velocity jet which is typical of Class 0 protostars. This brings into question whether it is steadily accreting in its current state, and if there is at all any definitive evidence of a jet. Therefore, L1527 is an ideal candidate to probe

¹ (Release ID 2022-055, PI: K. Pontoppidan) <https://webbtelescope.org/contents/news-releases/2022/news-2022-055>

the warm molecular and atomic jet emission using JWST MIR spectroscopy. Additionally, it is thought that the collimation and strength of the jets tends to decline with age of the protostar as the mass accretion rate decreases (e.g. Bontemps et al. 1996; Bally 2016). Hence, discerning L1527's outflow properties will be key to understand its evolutionary stage.

In this study, we present new results from JWST MIRI/MRS spectroscopic observations of L1527 covering the inner central region of 500 au. In Section 2, we give a brief overview of the instrument description and observational details. In Section 3, we show the results of the outflow spectra and spatial maps of different emission lines. In Section 4.1, we present physical properties of temperature and column density through excitation diagram analysis of H₂ lines with comparison to shock models. In Section 5, we discuss the results and presence of a jet. Finally, in Section 6 we present the summary and concluding remarks.

2. Observations

L1527 observations with JWST were obtained with the Mid-Infrared Instrument / Medium Resolution Spectrometer (MIRI/MRS; Rieke et al. 2015; Wright et al. 2023; Argyriou et al. 2023). The observations were part of a larger program called “JWST Observations of Young protoStars (JOYS)” (PID1290; van Dishoeck et al. 2025). The JOYS program observes a total of about 20 low to high-mass star-forming cores. The MIRI/MRS instrument does simultaneous spatial and spectral observations between wavelengths of 5 μm to 28 μm , covering a field of view of up to $\sim 7'' \times 7''$ with a spectral resolving power of $R \approx 3500$ to 1500. The instrument has 4 IFU channels with 3 grating sub-band settings (Short, Medium, Long). A full spectrum coverage requires exposure in each of the 3 sub-bands, resulting in 12 spectral segments. MIRI/MRS instrument achieves a PSF FWHM of $\sim 0.2''$ at 5 μm to $\sim 1''$ at 28 μm , corresponding to a physical scale of ~ 30 au to ~ 130 au at a distance of 140 pc, thereby providing coverage to the innermost region of L1527.

The science observations were carried out on March 4th, 2023 as part of Cycle 1 JOYS guaranteed time observations. The target position was centered on coordinates $4^{\text{h}}39^{\text{m}}53^{\text{s}}.955 +26^{\circ}03'09''56$ (J2000). This pointing is slightly offset from the protostar center ($4^{\text{h}}39^{\text{m}}53^{\text{s}}.87 +26^{\circ}03'09''58$) on purpose to cover a larger portion of the brighter eastern outflow lobe, but also still observing some part of the western lobe. The data were acquired using FAST1 readout mode with 180 groups of one integration per sub-band. The integration time per sub-band was 1000 s, which resulted in total integration time of 3000 s to obtain the full spectrum. A two-point dither pattern was implemented to cover the extended morphology of the target. Additionally, a dedicated background field was observed with no dithering and having the same target integration time.

The data were reduced from Stage 0 uncalibrated raw files (.uncal) with the JWST pipeline v.1.12.5 (Bushouse et al. 2023), using corresponding Calibration Reference Data System (CRDS) context file jwst1174.pmap. During Stage 1 process, the raw files were processed for detector level corrections using **Detector1 Pipeline** default settings. This included dark current removal, flagging of bad pixels, non-linearity correction, ramp jump corrections and readout noise removal, resulting in images with count rate per second. During Stage 2 process, the images were calibrated using the **Spec2 Pipeline** settings. Here, the data was processed for addition of WCS information, flat field correction, background subtraction, flux calibration and fringe correction including removal of residual fringes (Crouzet et al. 2025). An additional bad-pixel removal

routine was applied for outlier detection using the Vortex Image Processing (VIP) package (Christiaens et al. 2023). The absolute flux calibration was performed from observations of spectrophotometric standards to convert the detector image to units of MJy sr⁻¹ (Argyriou et al. 2023). Wavelength calibration is applied using MIRI/MRS reference files derived from lab measurements and observations of line emission from astrophysical standards. The wavelength scale is additionally corrected from the observatory reference frame to the barycentric reference frame. Finally, for Stage 3 process, **Spec3 Pipeline** step was applied which included spectral extraction and cube creation. Totally, 12 data cubes were created corresponding to each of the MIRI/MRS channel and sub-bands. The spectra of all 12 sub-bands were stitched together to allow for a single analysis of the full MIRI/MRS wavelength range.

Since the MIRI spectral cubes are calibrated in the barycentric reference frame, we applied a constant barycentric-to-LSR velocity correction of -10.1 km s^{-1} , appropriate for the coordinates of L1527 and the time of observation. In addition, the velocities were shifted to rest frame by correcting for the systemic velocity of $+5.9 \text{ km s}^{-1}$.

3. Results

3.1. General MIR imaging and spectral features

In Fig. 1, we present a mid-infrared three-color map of the L1527 region, taken using MIRI broadband filters in 5.6 μm , 7.7 μm and 12.8 μm (PID 1798: J. Tobin & PID 2729: K. Pontoppidan). This map, covering a large field-of-view, allows us to get an improved understanding of the outflow structure in the MIR compared to previous observations. The outflow and the cavity walls are clearly seen as a bright bipolar structure extending to about 6000 au in each direction. Several prominent nebulous filaments consisting of bow shocks, knots and reverse shocks which were unresolved in previous Spitzer MIR images (Tobin et al. 2008), are revealed in this new MIRI map. Some of the bright emission near bow shocks may be associated to UV irradiation. Many cavities are seen near the vicinity of bow shocks where gas and dust is swept away. The outflow is seen to be launched at a wide angle from within the inner 200 au region as previously observed and modeled (Tobin et al. 2008, 2013). Towards the central region, the outflow structure is bright, consisting of the bulk of the emission, whereas towards the wings and rear regions it is fainter. Overall, the outflow appears to be in the plane-of-sky with the eastern flow relatively brighter than the western flow.

The right panel in Fig. 1 shows a zoomed in view of the 500 au central region with brightness scaled to reveal the eastern and western outflow lobes. Both lobes have similar symmetrical morphology, with eastern lobe relatively brighter. The lobes are bisected by a dark lane at the center as expected from the edge-on-disk. The outflow lobes have a bright continuum emission which likely includes scattered light from the inner disk. The position of the forming protostar from millimeter continuum is marked by a star symbol. Two circular apertures in red and blue are shown positioned on the outflow lobes for the MIRI/MRS spectral extraction. The placement of the aperture position was determined such that it is close to the central protostar, but also covering the outflow emission. This would give us a better representation of the properties in the region. The aperture radius was set to $R_a = 0.033 \times \lambda + 0.106$, which at 5 μm is 0''.27 and at 20 μm is 0''.76. This is twice the size of MIRI FWHM PSF as characterized by Law et al. (2023).

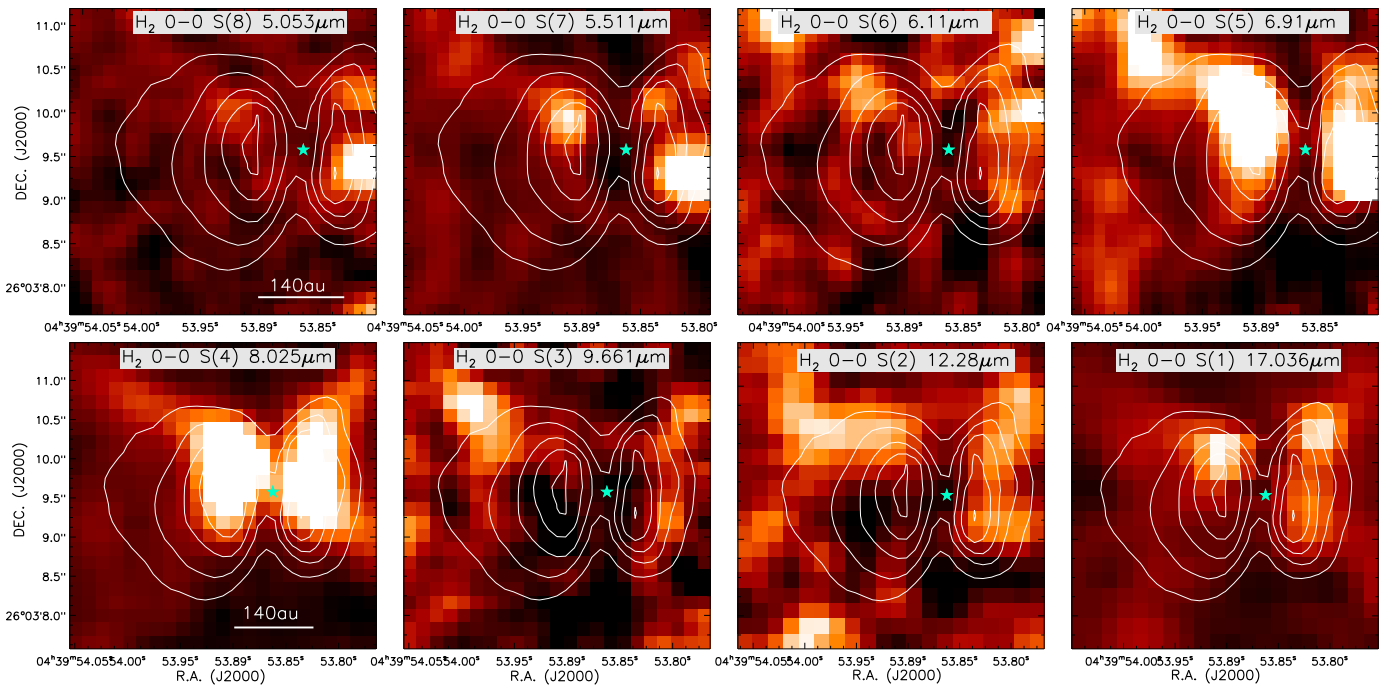


Fig. 3. Line integrated intensity (Moment 0) maps of molecular H_2 0-0 rotational transitions from S(8) to S(1) covering 5 – 28 μm range. The upper state excitation energies for H_2 are decreasing from S(8) to S(1) transitions (see Table 1). The maps are created after subtracting the local continuum. Brightest regions correspond to strongest H_2 emission. White contours shown are the 5.6 μm broadband emission. Position of the central star is shown as a star symbol.

The bottom panel in Fig. 1 shows the full distribution of the MIRI/MRS spectra extracted at the aperture positions. The color-coding of the spectra in red and blue correspond to the eastern and western lobes, respectively. Fig. 2 provides a more detailed view, separating the spectra into four panels corresponding to the four MIRI channels (Ch1, Ch2, Ch3 and Ch4), each observed with three grating settings. In general, the spectra are seen to increase in flux density with wavelength, which is typical for embedded protostars. However, there are several positions with strong absorption features which are characteristics of ices and silicates (Pontoppidan et al. 2008; Öberg et al. 2011; Yang et al. 2022). The ice features comprise of both simple (H_2O , CO_2 , CH_4) and complex organic molecules: COM (CH_3OH , $\text{C}_2\text{H}_5\text{OH}$) (Rocha et al. 2024; van Gelder et al. 2024). The most strongest absorption occur particularly between ~ 5 and $\sim 11.5 \mu\text{m}$. We also see few positions of sharp dip at around 7.7 and 15 μm due to CH_4 and CO_2 ice (Yang et al. 2022). These solid-state features are indicated by various colored bands in Fig. 2.

At longer wavelengths, the increase in flux density is steep as expected from the warm dust emission. Overall, the eastern and western lobe show a similar spectral energy distribution without any significant difference. Given, the high sensitivity of JWST even with short integration times we detect several spectral lines of molecular, atomic, and ionized emission towards both lobes. Pure rotational $\text{H}_2 \nu = (0-0)$ transitions were detected covering the entire MIRI wavelength range. Forbidden atomic and ionized emission lines of $[\text{Ni II}]$, $[\text{Ar II}]$, $[\text{Ne II}]$, $[\text{Ne III}]$, $[\text{S I}]$, and $[\text{Fe II}]$ were also detected. The spectra from the eastern region showed stronger intensities and presence of more ionized emission lines, which are discussed in Section 3.3.

3.2. Molecular Hydrogen emission

The MIRI/MRS spectral data cubes allow us to get a better understanding of the underlying outflow structures in L1527. Molecular hydrogen (H_2) is an excellent tracer of the bulk of the outflowing gas. These lines are primarily excited by shocks, with additional contributions from UV irradiation. The shock excitation exhibits range of characteristics. Traditionally, J -type shocks are fast and dissociative, while C -type shocks are slower and largely non-dissociative (Hollenbach & McKee 1989; Froebrich et al. 2003). However, the distinction between J - and C -type shocks depends not only on the shock velocity but also on the magnetic field strength and ionization fraction. In particular, slow J -type shocks with limited dissociation are possible under moderate magnetic fields (Kristensen et al. 2023). The H_2 emission can thus reflect a mixture of different shock conditions. The H_2 emission lines in the MIR are primarily due to rotational and rovibrational transitions (Caratti o Garatti et al. 2024; Tychoniec et al. 2024). In our observation we detect the optically thin pure rotational $\nu = (0-0)$ transitions from S(1) to S(8) as shown in Fig. 2. The S(0) line is not detected due to the poor MIRI/MRS sensitivity beyond 27 μm . We find that the S(7), S(5), and the S(4) are the brightest lines in the spectra. Table A.1 provides the list of all detected H_2 lines with their properties.

In Fig. 3, we present the continuum subtracted H_2 line integrated intensity (Moment 0) maps with the field-of-view covering the inner 500 au region. The general H_2 emission follows a bipolar morphology tracing the outflow structures. Transitions S(8), S(6), S(3), S(2), and S(1) are weak throughout the region with just few positions of detectable emission. Most of this is due to absorption from the ices and dust. The S(1) line appearing weak compared to higher excitation lines is particularly unusual and suggests that the emission is dominated by hot gas, pointing

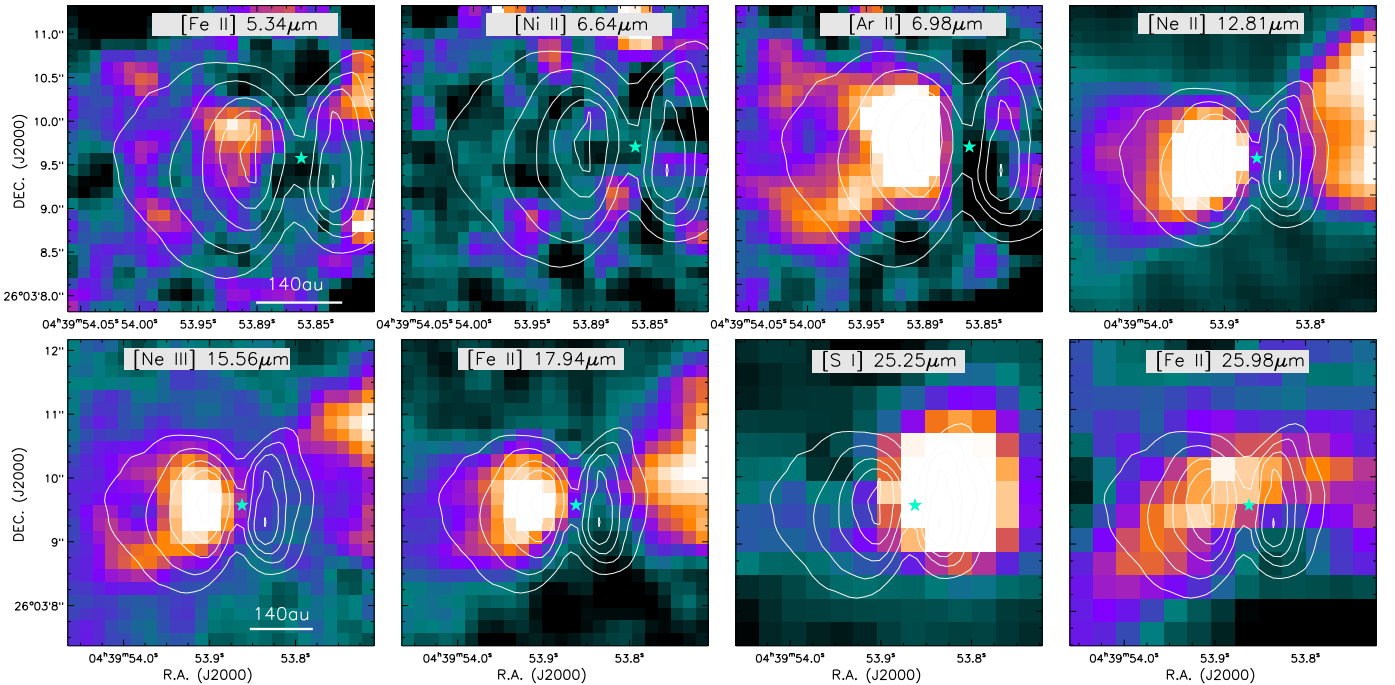


Fig. 4. Line integrated intensity (Moment 0) maps of atomic and ionized emission lines in L1527. The maps cover all the lines detected in the MIRI spectral range and are created after subtracting the local continuum. Brightest white-orange regions correspond to strongest line emission in each of the species. White contours shown are the 5.6 μm broadband emission. Position of the central protostar is shown as a star symbol.

to excitation by shocks. The S(7) transition shows moderately detectable emission in both the lobes.

Transitions S(5) and S(4) have the strongest emission closely matching the morphology seen in the broadband images. The emission originates near the base of the outflow lobes and expands with a wide opening angle, outlining a symmetrical parabolic structure on both sides. The boundaries of the outflow cavity walls are clearly defined in these transitions and extend radially beyond the 200 au region. The observed alignment likely reflects emission arising along the cavity walls, either from shocks or UV irradiation. While UV heating can affect the gas temperature, UV pumping primarily excites the vibrational levels of H_2 and has little impact on pure rotational transitions (e.g. Sternberg & Dalgarno 1989). Scattered H_2 emission is also expected to be negligible in the observations. While dust grains can scatter both continuum and line photons, dust scattering efficiencies at MIR wavelengths are generally low and are most significant in the NIR (e.g. Delabrosse et al. 2024). Moreover, the line-to-continuum ratio in the observations is relatively low, so even if H_2 photons are scattered, their contribution to the observed emission is weak. Although scattering can be more important in some edge-on disks, such as HH 30 (e.g. Tazaki et al. 2025), in L1527 the observed morphology and brightness indicate that direct H_2 line emission from the outflow cavities dominates. H_2 emission originating near the inner disk could in principle be scattered, but its expected contribution is also minor. More discussion on continuum scattered light is presented in Tobin et al. (2008, 2010).

There is no collimated feature in any of the H_2 maps that may otherwise be associated to a jet. This is consistent with previous longer wavelength molecular observations which were seen to have wide outflow morphology (Yildiz et al. 2015; van't Hoff et al. 2023). The majority of the H_2 emission appears to be associated with a single morphological component of the outflow,

most likely the outflow cavity itself. We do not observe any variation in the extent of the outflow opening angle with change in the upper energy levels between each transitions. This behavior contrasts with that observed in TMC 1-E (Tychoniec et al. 2024). The similarity in the spatial extent of all the H_2 emission suggests a common origin within the outflow, although multiple excitation conditions may coexist within this region.

The overall excitation of the H_2 emission is most likely driven by shocks and by shock-generated UV radiation, while direct stellar UV irradiation is unlikely to contribute significantly due to multiple constraints. Given that L1527 is a deeply embedded, low-mass protostar ($\sim 0.3 \text{ M}_\odot$), the intrinsic stellar UV field is weak and can be heavily attenuated by the dense outflow and envelope ($\sim 1.0 \text{ M}_\odot$), making direct UV irradiation of H_2 negligible. Moreover, there is no nearby massive star in the surrounding environment that could provide an external UV field. While some UV photons may preferentially escape along the outflow cavity, they would rapidly dilute long before reaching the spatial scales of the outflow ($> 5000 \text{ au}$). The outflow morphology shows multiple discrete knots and bow-shaped structures aligned with the jet/outflow axis that are characteristic of local collisional excitation rather than irradiation by a distant, centrally located source. Further evidence against a UV-dominated environment is the absence of the clearly observed 11.2 μm PAH emission with JWST (e.g., Beuther et al. 2023). These factors together imply that large-scale UV irradiation cannot dominate the H_2 line emission. Shocks from the disk wind and jets play a significant role in H_2 emission. Comparison of the observed data with H_2 shock models (Kristensen et al. 2023) demonstrates that moderate velocity J -shocks with modest UV field values appear to be most consistent with our results (see Section 4.2).

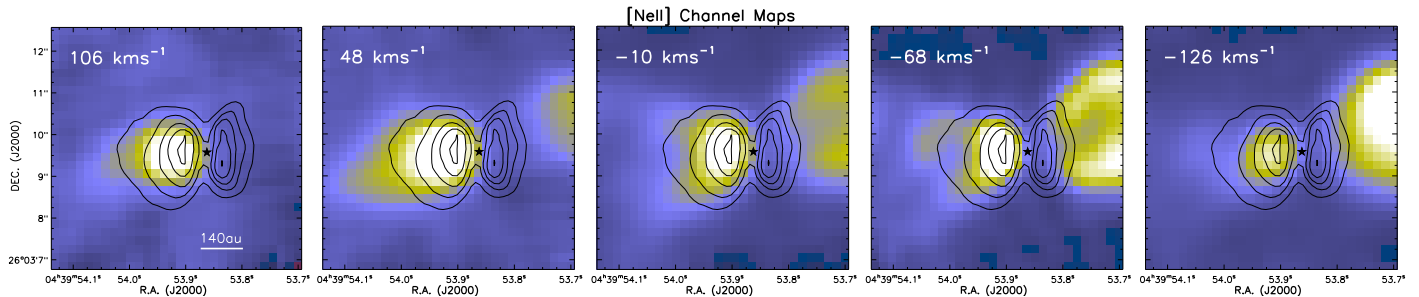


Fig. 5. Channel map of $[\text{Ne II}]$ $12.813\,\mu\text{m}$ continuum subtracted emission in L1527. The maps span radial velocity ($V_{\text{rest,LSR}}$) interval between $-126\,\text{km}\,\text{s}^{-1}$ to $106\,\text{km}\,\text{s}^{-1}$. Extended emission tracing the outflow on both the lobes is seen. Black contours shown are the $5.6\,\mu\text{m}$ broadband emission. Position of the central protostar is shown as a star symbol.

3.3. Atomic and Ionized Lines

Atomic and ionized species are useful to trace various physical components within the outflow environment. Their emission reveals the underlying process involved in excitation of these species (Neufeld et al. 2009; Beuther et al. 2023; Gieser et al. 2023). This is the first time several emission lines in the mid-infrared have been observed in the L1527 outflow. As shown in Fig. 2, we detect $[\text{Ni II}]$, $[\text{Ar II}]$, $[\text{Ne II}]$, $[\text{Ne III}]$, $[\text{S I}]$, and $[\text{Fe II}]$ emission lines. Table A.2 provides properties of the detected atomic and ionized lines.

In Fig. 4, we present the continuum subtracted line integrated intensity (Moment 0) maps. The $[\text{Fe II}]$ ($5.34\,\mu\text{m}$) and $[\text{Ni II}]$ ($6.64\,\mu\text{m}$) maps have very faint emission without any significant morphological details. Noble gases of $[\text{Ar II}]$, $[\text{Ne II}]$, and $[\text{Ne III}]$ show the most prominent emission in the maps tracing the outflow structures. Their origin could be due to high energy shocks from the outflow or through photoionization from UV radiation. The $[\text{Ar II}]$ map shows a predominantly bright emission in the eastern lobe. This emission is distributed similarly to the H_2 S(5) emission, with both species excited at nearby central wavelengths. The bright $[\text{Ar II}]$ emission could be tracing the outflow cavity as well as the shocked material from the entrained ambient gas, reflecting an increase in ionization towards the eastern flow. On the other hand, there is almost no detection on the western lobe, suggesting that the shocked material has already been cleared up or is further away from the central region.

In the $[\text{Ne II}]$, and $[\text{Ne III}]$ maps, we observe the full extent of the outflow material on both lobes. The emission exhibits a clear bipolar distribution, expanding outward along the direction of the outflow. On the eastern side, the emission remains closely aligned with the continuum and is more uniformly distributed along the outflow axis. However, on the western side the emission becomes significantly brighter only beyond a distance of approximately 150 au from the central protostar, suggesting asymmetry in the excitation conditions or variations in the density of the medium. The presence of both $[\text{Ne II}]$, and $[\text{Ne III}]$ emission indicates there are multiple ionization layers in the outflow, with the $[\text{Ne III}]$ requiring higher energies for ionization. We discuss in Section 3.4 further details on the $[\text{Ne II}]$ emission.

The $[\text{Fe II}]$ emission at $17.94\,\mu\text{m}$ and $25.98\,\mu\text{m}$, both show the outflowing shocked material similar to the $[\text{Ne II}]$ morphology. However, the emission at $25.98\,\mu\text{m}$ is much fainter and is affected by poorer resolution. The outflowing material seen here is not symmetric around both lobes. We see that the western ejection is much stronger and expands slightly northwards when compared to the H_2 emission. This is also not observed in the broadband images. Most of the $[\text{Fe II}]$ emission mainly traces the

warm shocked gas. It is likely arising from dissociative shocks at low excitation energy levels (Neufeld et al. 2009).

The $[\text{S I}]$ line is the only neutral atomic emission we detect in our observations, unlike other JOYS sources which have in addition detected $[\text{Cl I}]$, and $[\text{Fe I}]$ (e.g. HH 211; Caratti o Garatti et al. 2024). The $[\text{S I}]$ map shows distinctively bright emission in the western lobe. The emission is not collimated and appears spatially extended. There is no significant $[\text{S I}]$ emission towards the eastern lobe, in contrast to the ionized lines, which exhibit stronger emission there. The prominent $[\text{S I}]$ emission therefore most likely reflects different ionization conditions between the two outflow lobes, with the western lobe containing predominantly neutral gas. Such neutral conditions naturally favor excitation of the $[\text{S I}]$ line and are consistent with slow, partially dissociative J -shocks in dense gas (Hollenbach & McKee 1989; Neufeld et al. 2007). In such environments, the enhanced $[\text{S I}]$ emission does not require a separate dust-destruction mechanism but instead is produced by shock-excited neutral gas in which the ionization fraction is considerably lower.

3.4. $[\text{Ne II}]$ line analysis

The mid-infrared fine-structure line of $[\text{Ne II}]$ at $12.81\,\mu\text{m}$ is an excellent tracer of gas in outflows and disks. In outflows the line is thought to be excited by high velocity dissociative shocks of the ambient gas or through UV/X-ray photoionization. In Class II disks it has been observed to originate mainly by heating and ionization through stellar X-ray and UV radiation (Hollenbach & McKee 1989; Pascucci et al. 2009; Güdel et al. 2010). The distance from the central protostar to the emission location generally determines their excitation condition.

The $[\text{Ne II}]$ line exhibits one of the strongest emission among all the detected lines. As shown in the Moment 0 map (Fig. 4), the emission traces the characteristic structure of a bipolar outflow. However, the morphology of the emission is not symmetric spatially on both the lobes. On the eastern region, most of the emission is focused near the outflow lobes. In contrast, on the western side, the emission appears fainter near the protostar but becomes significantly stronger beyond a distance of ~ 150 au. Additionally, the emission on the western side shows flow moving slightly northwards, consistent with the morphology observed in the $[\text{Fe II}]$ maps.

In Fig. 5, we present the $[\text{Ne II}]$ continuum subtracted channel maps at different radial velocities ($V_{\text{rest,LSR}}$ between -126 to $106\,\text{km}\,\text{s}^{-1}$). Each panel corresponds to the minimum spectral interval ($\sim 0.0025\,\mu\text{m}$) of the MIRI datacube. We see that on the eastern region there is predominantly bright emission on the outflow lobe across all velocity range. This emission is very close to

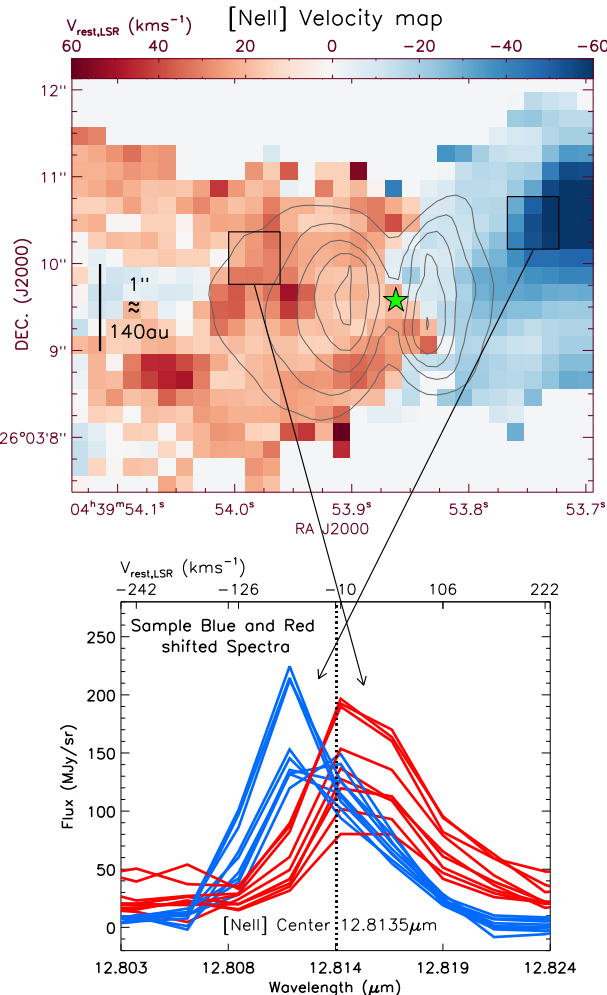


Fig. 6. The top panel shows $[\text{Ne II}]$ radial-velocity ($V_{\text{rest,LSR}}$) map of the L1527 region. The map is created by Gaussian fitting the $[\text{Ne II}]$ line and estimating the doppler shifted velocity in each spaxel. Black contours shown are the $5.6\ \mu\text{m}$ broadband emission. The bottom panel shows sample red and blue shifted spectra for a box region of 3×3 pixels in the eastern and western regions. The central $[\text{Ne II}]$ wavelength is shown by a dotted vertical line.

the protostar and most likely tracing the outflow wind. In addition, there is a faint extended emission in the vicinity that could arise from the outflow cavity walls.

On the western side, we see a clear bright emission at blue shifted velocities. As we move from red shifted to blue shifted velocities, the strength of the emission increases progressively and highlights the different sections in the $[\text{Ne II}]$ emission. Most notably, the emission at higher blue shifted velocities appears brighter farther away from the protostar. At about 250 au away from the protostar, we see a bright blob of shocked emission suggesting that the dense gas in the ambient medium has been ionized by high velocity flows. Such type of emission is predicted to arise from J -shocks with high shock velocities (Hollenbach & McKee 1989). It is also predicted that the $[\text{Ne II}]$ intensities increase with presence of high density material, which may correspond to our results. Overall, we see that the $[\text{Ne II}]$ emission is traced at multiple regions from near to far from the protostar indicating its origin being predominantly shocks.

In Fig. 6, we present the radial velocity map derived from the $[\text{Ne II}]$ emission lines. To obtain this map, we performed 1-

Dimensional (1-D) Gaussian fits to each pixel in the datacube and estimated the radial velocity of the line, shifted to the rest frame in LSR. We set a minimum threshold of $10\ \text{MJy sr}^{-1}$ for the Gaussian fits in order to ensure reliable velocities from high SNR lines. In the bottom panel of Fig. 6, we present sample spectra for a box region of 3×3 pixels to show the distribution of the red and blue shifted spectra with respect to the $[\text{Ne II}]$ central wavelength. The resulting velocity map clearly shows the region to be distributed into two outflow components: the red and blue shifted regions. Both velocity components appear to bifurcate near the location of the central protostar, supporting the interpretation that the outflow is oriented close to the plane-of-sky. This is consistent with previous estimates of inclination of $i \approx 75 - 85^\circ$. There is also a slight presence of red shifted emission in the western lobe close to the protostar, which may be due to orientation or projection effects.

The direction of propagation of the outflow material is not strictly along the horizontal axis. Instead, the blue shifted region is observed to move north-west consistent with the direction seen in other ionized emission lines. This type of morphology is not apparent in the broadband images or in the H_2 emission maps, suggesting that the molecular and ionized emission are tracing different layers of the outflow. The average velocity in the blue and red shifted region is about $-24 \pm 8\ \text{km s}^{-1}$ and $28 \pm 11\ \text{km s}^{-1}$, respectively. The red shifted region appears uniformly distributed without any significant velocity gradient along the flow. In contrast, the blue shifted region shows a sharp increase in velocity with distance from the protostar, consistent with the flow structure observed in the channel maps (Fig. 5). Additionally, a vertical velocity gradient is evident in the blue shifted region, suggesting the presence of emission from multiple layers. The lower blue shifted velocities at the outer edges likely trace the outflow cavity wall, whereas the central brighter blue shifted feature appears to originate from shock-heated gas.

The most interesting feature of the velocity map is the distribution of red shifted and blue shifted velocities, which appear associated with the eastern and western regions, respectively. This completely contrasts few earlier studies (Hogerheijde et al. 1998; Tobin et al. 2008), which suggested that the eastern side is blueshifted and the western side is redshifted. Yildiz et al. (2015) conducted ^{12}CO observations in the 3-2 and 6-5 transitions and reported that the $^{12}\text{CO}(3-2)$ maps predominantly showed blue shifted velocities on the eastern side. However, in the $^{12}\text{CO}(6-5)$ transition, they observed the opposite, the western side being blue shifted. This mixed velocity distribution was attributed to the large opening angle of the outflow and its orientation nearly in the plane-of-sky.

High-resolution ALMA observations by Oya et al. (2015) using CS rotational lines, a dense gas tracer, provided a clearer kinematic picture. Their position-velocity diagram analysis suggested that the western side of the outflow is blue shifted while the eastern side is red shifted, consistent with our findings in the $[\text{Ne II}]$ velocity map. We also performed velocity analysis for other MIRI ionized lines and obtained a similar result. This result is somewhat counterintuitive in the context of scattered light continuum where the eastern side appears brighter than the western side (Tobin et al. 2008, 2010). Typically, dust scattering is brighter on the side of the disk tilted towards the observer. Recently, van't Hoff et al. (2023) showed there was brightening on the eastern side suggesting the extended disk being inclined towards the observer. However, given the flared and asymmetric nature of the disk, the inner disk may still not be tilted towards the observer. Thus, the discrepancy between the scattered light observations and the kinematic structure revealed by

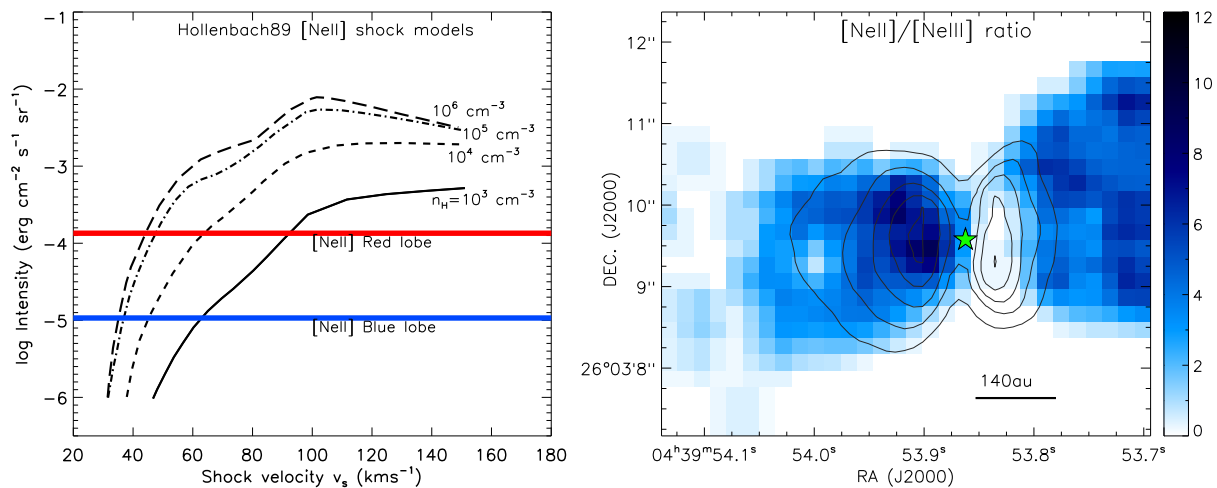


Fig. 7. Left: [Ne II] emission compared to [Hollenbach & McKee \(1989\)](#) *J*-type shock models with range of predicted intensities against pres-shock densities and shock velocity. Observed line intensities are highlighted in red and blue, which are obtained at aperture positions in the eastern and western lobe (see Table A.2). Right: [Ne II]/[Ne III] ratio map obtained from continuum subtracted and extinction corrected line intensities.

the [Ne II] maps suggests that the dust distribution may not be perfectly aligned with the true inclination of the disk. Further, the MIRI/MRS data provides high-resolution spectral imaging in the innermost regions, and are less susceptible to biases from large-scale wide morphological orientation. Therefore, our results taken together with the jet orientation (see Section 5) likely represents the true orientation of the outflow, with the eastern side associated with red shifted velocities and the western side with blue shifted velocities.

3.5. [Ne II] shock model and [Ne II]/[Ne III] ratio map

[Hollenbach & McKee \(1989\)](#) presented detailed models of *J*-type shocks which produce strong atomic and ionic emission due to the fast, dissociative heating at the shock fronts in the absence of significant magnetic field. In particular, the model predicts bright [Ne II] emission from high velocity shocks, that is sensitive to pre-shock density and shock velocity.

To assess whether *J*-shocks can account for the observed [Ne II] emission in L1527, we compared the models to our continuum-subtracted and extinction corrected [Ne II] line intensities obtained at aperture positions along the eastern and western outflow lobes. The left panel in Fig. 7 shows the comparison red and blue solid lines plotted against pre-shock density and shock velocity. The models that best reproduce the measured intensities correspond to shock velocities of approximately 35 to 45 km s⁻¹ at pre-shock volume densities of $\sim 10^4 - 10^5 \text{ cm}^{-3}$, which is typical densities expected in the dense envelope of L1527. This agreement supports the interpretation that moderate velocity dissociative *J*-type shocks are operating in the outflow, producing sufficient ionization to power the observed [Ne II] emission.

The [Ne II]/[Ne III] line ratio is widely used to diagnose the ionization state and hardness of the radiation or shock environment ([Güdel et al. 2010; Shang et al. 2010](#)). Since [Ne II] (ionization potential 21.56 eV) traces singly ionized gas, while [Ne III] (41.96 eV) requires much higher-energy photons or strong collisional ionization, their ratio is sensitive to both the ionizing spectrum and the electron temperature/density in the emitting gas. Low ratios (<1) are typically associated with highly ion-

ized environments such as fast dissociative shocks ($> 80 \text{ km s}^{-1}$) or strong FUV/EUV radiation fields, whereas high ratios (>2) indicate predominantly singly ionized gas, either due to softer radiation, slower shocks, or efficient recombination in dense regions. This ratio therefore provides a valuable constraint on the physical conditions and excitation mechanism of the gas.

We constructed a spatially resolved [Ne II]/[Ne III] ratio map using continuum subtracted and extinction corrected line intensities across the field. The right panel in Fig. 7 shows the image of the ratio map. The values range predominantly between 3 – 10, indicating that [Ne II] emission clearly dominates over [Ne III] throughout the outflow. Ratios in this range are consistent with moderately ionized, dissociative *J*-shocks where the ionization fraction is significant but not high enough to produce strong [Ne III] emission, thereby supporting a shock driven excitation rather than a hard stellar UV/X-ray source ([Hollenbach & Gorti 2009](#)). Moreover, the spatial structure of the ratio map shows particularly enhanced values at few positions of knots/shocks, that may indicate high density regions or contribution from soft ionization produced by shock-generated UV radiation. In the next Section 3.6, we reveal the identification of a high-velocity (HV) component in the ionized lines indicating the presence of a fast jet. If the [Ne II]/[Ne III] ratio is evaluated specifically for the HV component, the ratio falls to values $\lesssim 1$. This behavior arises because the HV component is barely detected in [Ne II], while clearly present in [Ne III], indicating that the [Ne III] ionization is predominantly associated with the fast jet (with velocities $> 80 \text{ km s}^{-1}$). This implies different excitation regimes within a stratified jet-outflow structure, where fast, highly ionizing shocks in the jet produce [Ne III], while moderate, partially ionizing shocks and shock-generated UV fields in the cavity produce the dominant [Ne II] emission.

3.6. Double peak lines: Jet detection

Double-peaked spectral lines in protostars are linked to complex geometries and kinematics. These lines typically arise from Doppler-shifted emission caused by fast moving flows with their components moving at different velocities. High-resolution observations of many protostars have shown that forbidden emis-

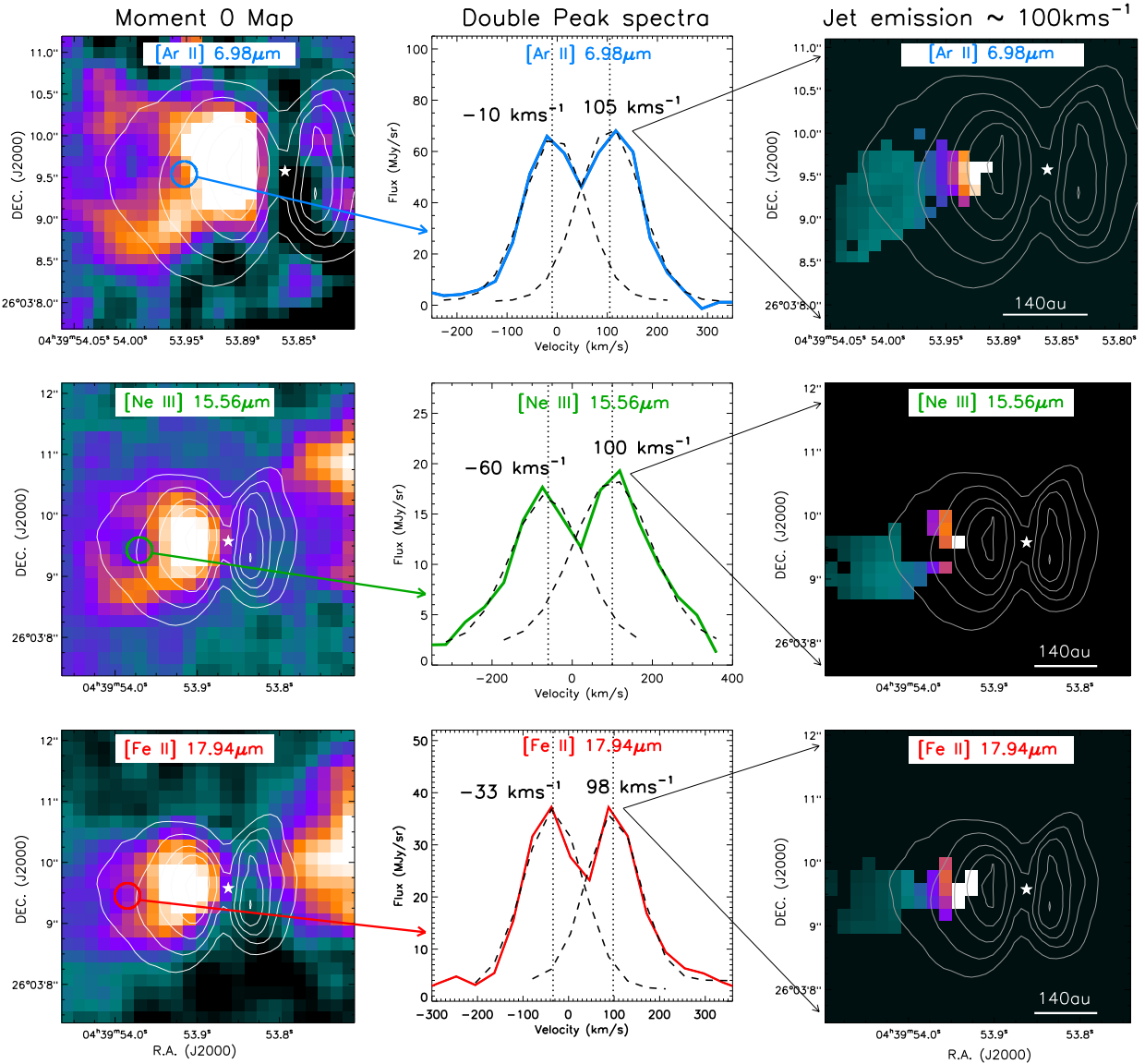


Fig. 8. Double peak emission observed in [Ar II], [Ne III], and [Fe II] emission lines. The first column of three panels show Moment 0 map of the lines with aperture positions that cover sample pixels with double peak emission. The middle column of three panels shows the spectra of a double peak emission line in blue, green and red for [Ar II], [Ne III], and [Fe II] respectively. 1-D Gaussian fits to each velocity component are shown in dashed lines. The estimated radial velocity values of the low and high velocity components are indicated. The last column of three panels shows the distribution of high velocity component associated to the jet emission. Brightest white-orange regions correspond to strongest jet emission.

sion lines often exhibit two velocity components, namely the low-velocity (LV) and high-velocity component, see review by Eislöffel et al. (2000). Such velocity separations can also arise in bow-shock structures, where a curved shock front produces a range of shock velocities and spatially separated emission regions (Hartigan et al. 1987). These interpretations have been supported by theoretical simulations with magnetohydrodynamic (MHD) jet models (Garcia et al. 2001; Shang et al. 2002). They have shown through their position-velocity diagrams the presence of different velocity components.

Closer inspection of the L1527 MIRI/MRS spectra reveals clear double peak emission in three different forbidden lines: [Ar II], [Ne III], and [Fe II]. The [Ne II] line showed very weak and un-resolved profile limited to just few pixels and was therefore excluded. The double peak emission was detected only on the eastern region of the outflow. Fig. 8 shows the profiles and the

morphology of double peak spectra for [Ar II], [Ne III], and [Fe II] lines. In the first column, the Moment 0 maps are presented with the sample aperture positions. In the middle column, we show the double peak spectra extracted at the sample aperture position. The spectra are color coded blue, green, and red for [Ar II], [Ne III], and [Fe II], respectively. The line profiles clearly show two separate velocity peaks associated to LV and HV components. A 1-D Gaussian fit was performed on each velocity component to estimate their peak radial velocity, shifted to the rest frame in LSR. In the last column of Fig. 8, we show the jet emission map associated to the HV component. The jet emission was isolated from the double-peaked line profile by extracting the high-velocity (HV) component, thereby identifying the spatial region associated with it. This was achieved by integrating the line intensity over a velocity range of $80 - 150 \text{ km s}^{-1}$, with an additional criteria that the emission exhibited a Gaussian profile

and a line width exceeding the spectral resolution. All the three maps show an extended jet with its brightest emission closest to the protostar.

The LV component observed in the double peak lines is distributed throughout the region and associated to the shocked gas in the general outflow or disk wind. The average radial velocity of the LV component is about -30 km s^{-1} , which is notably blue shifted. However, we can confirm that in regions without double peaked profiles, the average radial velocity is red shifted and is consistent with the [Ne II] velocity maps. Disk winds launched from few to several au's from the protostar are expected to have velocities of tens of km s^{-1} (Pudritz et al. 2007; Shang et al. 2007). They are thought to shape the molecular outflow cavities by sweeping up surrounding envelope material. Our observed LV component velocities are consistent with these predictions and supports previous studies indicating that the L1527 outflow cavity is shaped by a slow, disk wind entraining the ambient material (Tobin et al. 2008, 2012).

The double peak HV component is present only in the eastern region of the outflow. The [Ar II] line shows the strongest emission among the three detected lines. The average radial velocity of the HV component is about 100 km s^{-1} . The emission is not narrow/collimated, rather it is extended in width and follows the direction of the outflow axis to about 500 au. We see that the emission bends/curves towards the south in all the three maps. The HV component is interpreted as tracing the presence of a jet. Although the emission is not strictly collimated as seen in other Class 0/I jets, its observed velocity ($\sim 100 \text{ km s}^{-1}$), extended scale, and detection in high-ionization lines ([Ar II], [Ne III]) strongly suggest shock-excited jet activity, a strong characteristic of early-stage protostellar evolution.

Considering the jet is almost in the plane-of-sky, we can correct the radial velocity for inclination. For a value of $i \approx 75^\circ$, we get the true velocity to be around 385 km s^{-1} . This value should be interpreted cautiously as the disk is warped and the jet inclination would vary significantly due its precession/bending. Very high velocities ($>200 \text{ km s}^{-1}$) are predicted by magneto-centrifugal launching models when jets originate very close to the protostar. X-wind models (Shu et al. 2007), which launch material near the co-rotation radius, naturally produce such high velocities due to the strong gravitational potential in this region. However, disk-wind models (Ferreira 1997) can also generate comparably high velocities when launched from sub-au radii. Therefore, the large velocities observed in the jet likely indicates that its launching region lies very close to the protostar. Overall, the coexistence of both velocity components in multiple ionized lines suggests L1527 is composed of a stratified layer of gas with varying excitation conditions.

4. Excitation diagram analysis

4.1. Temperature and Column density maps

The physical properties like gas temperature T_{H_2} , and the column density $N(\text{H}_2)$ can be inferred using excitation diagram analysis of H_2 rotational transitions. The observed extinction-corrected H_2 line integrated intensities are converted into upper state column densities normalized by its statistical weight (N_u/g_u). These are plotted in a logarithm scale against their upper state excitation energies (E_u/k_B). For gas in local thermal equilibrium (LTE), the gas excitation follows a Boltzmann distribution ($N_u/g_u \propto \exp(-E_u/k_B)$) and the data points in the diagram can be fitted with a straight line. The gas excitation temperature is derived as the reciprocal of the slope of the line, whereas the

column density is proportional to the y-axis intercept. This analysis assumes that all H_2 transitions are optically thin, which is valid even for $N(\text{H}_2) > 10^{23} \text{ cm}^{-2}$ (Bitner 2008).

The MIRI/MRS spectral range covers several pure rotational H_2 transitions from the S(8) to S(1) state, which are detected in most pixels in the entire field-of-view. This allows us to carry out pixel-by-pixel excitation diagram analysis and to obtain a complete map of T_{H_2} , and $N(\text{H}_2)$. We first smooth the spectral cubes from different MIRI channels to the lowest common resolution as the angular resolution varies from $0\farcs2$ to $1\farcs0$ between all the MIRI channels. We smooth the spectral cubes to a resolution of $0\farcs7$ that corresponds to the S(1) transition, which is the lowest angular resolution in the detected H_2 lines. We also regrid the cubes to the same spatial grid as the H_2 S(1) data.

Next, we correct for extinction along the line-of-sight. The most commonly used extinction correction in MIR comes from McClure (2009) and KP5 (Pontoppidan et al. 2024) curves, with the latter introducing slightly stronger absorption from ices and silicates. Previous analysis of other JOYS sources adopted the McClure (2009) extinction curve that is valid between a K -band magnitude of $A_K = 1$ to 7 mag. However, recent study on ices in L1527 by Slavicska et al. (2025) showed substantial ice and silicate absorption, indicating that the KP5 curve provides a more appropriate extinction correction, which we apply in the analysis. The optical depth at $9.7\mu\text{m}$ was earlier estimated to be around $\tau_{9.7} \sim 4$ (Slavicska et al. 2025). We also measured the extinction by de-reddening the S(1) to S(8) lines on excitation diagram analysis, which yielded $A_K = 7$ mag (see Fig. B.2). Based on these results, as well as comparing previous extinction derived with SED modeling (Tobin et al. 2008, 2010), we adopt a value of $A_K = 7$ mag, that is roughly equivalent to a visual extinction of $A_V \approx 50$ mag. We tested lower extinction values between $A_K = 4 - 6$ mag and found that the intensity of the S(3) line decreases significantly and gets excluded in the fitting. We also find that an H_2 ortho-to-para ratio of 3 provides the best fit to our observed line intensities, assuming the H_2 gas is in LTE.

The excitation diagram analysis is performed using the `pdrtypy`² python package, which is commonly employed in the analysis of JOYS sources (Gieser et al. 2023; Caratti o Garatti et al. 2024; Francis et al. 2025). Typically, the observed H_2 rotational transitions trace two temperature components, often parameterized as a ‘warm’ and a ‘hot’ component in excitation diagrams. The warm component ($T_{\text{warm}} \approx 200 - 1000 \text{ K}$) is traced by the lower-excitation lines (e.g., S(0)-S(4), $E_{\text{up}} \leq 4000 \text{ K}$) and is commonly associated with slow, nondissociative C-shocks or the cooler post-shock gas within J -shocks. The hot component ($T_{\text{hot}} \approx 2000 - 3000 \text{ K}$), traced by the higher excitation transitions (e.g., S(5) and above, $E_{\text{up}} \geq 5000-10000 \text{ K}$), arises mostly from energetic fast dissociative J -shocks where collisional heating dominates. However, recent shock models (e.g., Kristensen et al. 2023) demonstrate that a single shock structure can produce both temperature components, where hot gas represents post-shock region and the warm gas traces the cooling layer of the same shock. Therefore, the presence of two temperature components does not necessarily indicate separate shocks, but can instead reflect a thermally stratified region with distinct excitation conditions. In general, the warm component typically carries most of the H_2 luminosity and therefore remains a dominant

² `pdrtypy` is developed by Marc Pound and Mark Wolfire. This project is supported by NASA Astrophysics Data Analysis Program grant 80NSSC19K0573; from JWST-ERS program ID 1288 provided through grants from the STScI under NASA contract NAS5-03127; and from the SOFIA C+ Legacy Project through a grant from NASA through award #208378 issued by USRA.

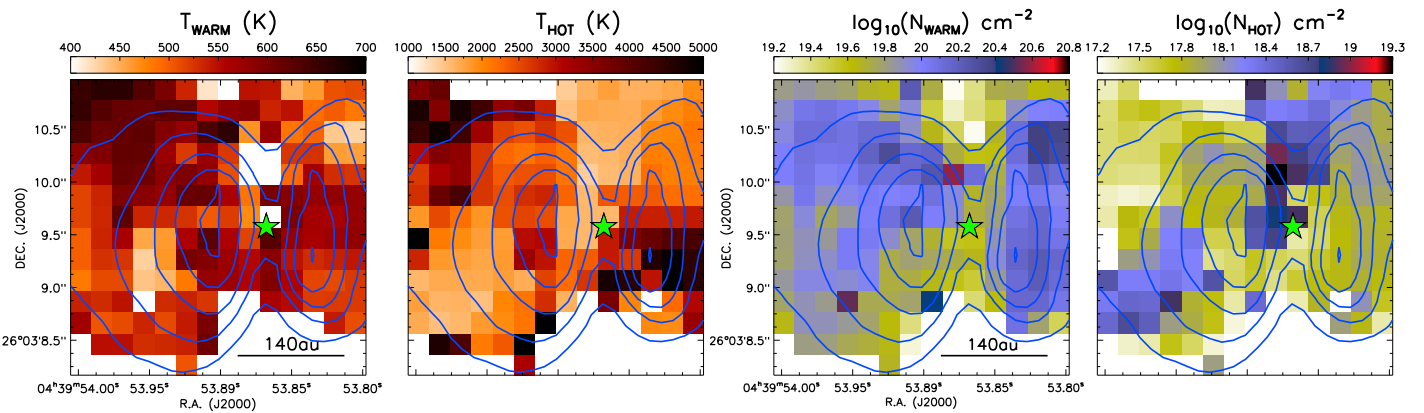


Fig. 9. Results of H_2 excitation diagram analysis for L1527, obtained by applying the analysis to each spaxel across the entire region. Left panels show temperature maps of the warm and hot gas components, and right panels show the corresponding column density maps. Color bars above each panel indicate the value ranges. Blue contours show the $5.6\text{ }\mu\text{m}$ broadband emission, and the central star is marked with a star symbol.

tracer of the bulk outflowing gas, while the hot component highlights localized regions of strong shock activity.

At the initial step, the extinction corrected H_2 transitions at each spaxel are fitted by a 1-D Gaussian and the line intensities are computed from the integral of the Gaussian fit. We set an intensity threshold of 20 MJy sr^{-1} to avoid any spurious detection. In Fig. B.1, we show example spectra for spaxels associated to the apertures in the eastern and western lobes (see Fig. 1). The spectra are plotted for different H_2 transitions and their Gaussian fits are highlighted in red and blue for eastern and western lobes, respectively. We see that the line intensities vary in value across different transitions depending on their strength. In general, lines from all transitions have bona fide profiles for the Gaussian fits without any omission.

Next, the line intensities from the spectra are converted to upper state column densities and are then plotted against their excitation temperature as described earlier. To have reliable estimates from the excitation diagram, fitting is performed only if five or more transitions are detected in a spaxel. Fig. B.3 shows the excitation diagram for the example spaxels in the eastern and western lobes. The data points with error bars are the upper state column densities of lines in each H_2 transitions. They are distributed across the plot with overlay of two fits in red and blue comprising of the warm and hot component. The total fit on the data points is shown as a solid green line. The estimated warm temperature in both the spaxels is similar, with an average of about $T_{\text{warm}} \approx 570\text{ K}$. Whereas, the hot temperature varies considerably with values of $T_{\text{hot}} \approx 2170\text{ K}$ and 3340 K for eastern and western spaxels, respectively. The estimated warm and hot column density in both the spaxels average about $N(\text{H}_2)_{\text{warm}} \approx 16 \times 10^{19}\text{ cm}^{-2}$ and $N(\text{H}_2)_{\text{hot}} \approx 9 \times 10^{17}\text{ cm}^{-2}$.

Fig. 9 presents the full temperature and column density maps for both the warm and hot components. In the temperature maps, the warm component exhibits moderate temperature variations across the outflow region, with values ranging between $450 - 650\text{ K}$. There is a noticeable gradient in the eastern lobe with increasing temperature towards north-east. This gradient closely follows the spatial distribution of the H_2 emission, particularly resembling the brighter S(5) and S(4) transitions (see Fig. 3). This suggests that there is presence of warm gas inside the outflow cavity. The western lobe also has a gradient, but with increasing temperature towards south-west and with lesser resemblance to the H_2 emission. In the hot component map, the temperature variations are substantial ranging

between $1500 - 5000\text{ K}$. Both sides of the region exhibit sharp increase in temperature along the outflow structures, closely resembling the distribution of the H_2 emission. These temperature variations and their spatial resemblance to the outflow morphology suggest that the heating of the gas is strongly linked to a common excitation mechanism within the outflow.

The column density maps exhibit a morphology broadly similar to the temperature maps. The warm component of the column density ranges from $N(\text{H}_2)_{\text{warm}} \approx 2 - 70 \times 10^{19}\text{ cm}^{-2}$, whereas the hot component ranges from $N(\text{H}_2)_{\text{hot}} \approx 2 - 100 \times 10^{17}\text{ cm}^{-2}$. The warm component is significantly denser, about two orders of magnitude higher than the hot component. In the warm component maps, regions of higher column density show a general positive correlation to regions with higher temperature. However, this is in contrast in the hot component maps, where regions of lower column density are seen to present higher temperatures. These trends likely reflect the nature of shock heating in the outflow.

In both the temperature and column density maps, we do not find any evidence of a jet based on the spatial variations or gradients at the position of the HV component (see Fig. 8). This lack of jet temperature or density signature is consistent with the absence of a molecular jet in our H_2 maps. Overall, the gas temperature and column density maps exhibit a strong correlation with the outflow morphology, suggesting that the outflow cavity is composed of layers of warm and hot gas.

4.2. Comparison to shock models

The H_2 emission from outflows in dense regions ($> 10^5\text{ cm}^{-3}$) is generally thought to be dominated by collisional excitation from shocks. However, UV driven irradiation may still play a role if accretion-generated UV photons penetrate the base of the outflow cavity before being attenuated, or if fast dissociative shocks generate local UV fields that modify the shock structure and chemistry. The strong gradients in temperature, density, and ionization across shock fronts naturally produce multiple excitation components, with hotter gas populating higher energy rotational states and warmer gas dominating lower levels. In order to constrain the mechanism of excitation in the outflow, we compare our observed H_2 emission with recent shock models that self-consistently treat different excitation processes.

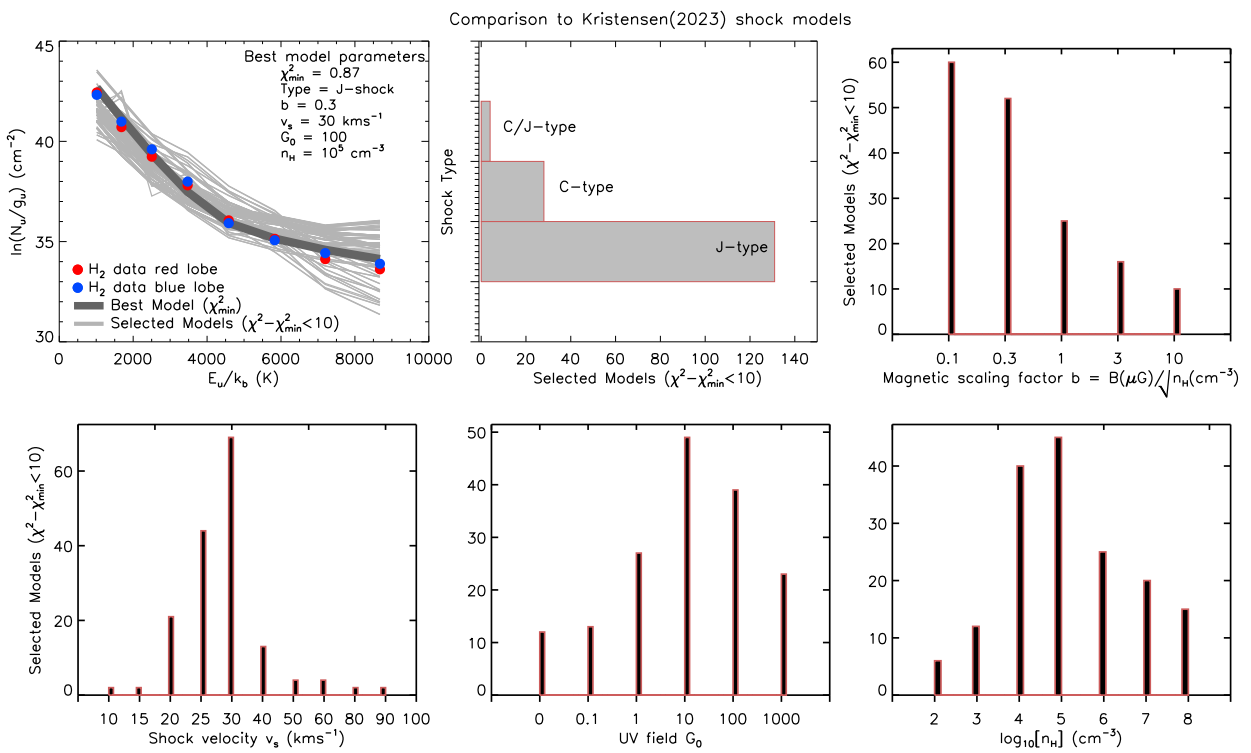


Fig. 10. Top left panel shows comparison of extinction-corrected H_2 rotational lines to Kristensen et al. (2023) shock models. The best model with χ^2_{\min} is shown in dark grey solid lines with its parameters displayed. The selected models with $\chi^2 - \chi^2_{\min} < 10$ are overplotted with light grey lines. Subsequent panels show histogram distribution of key model parameters (Shock type, Magnetic scaling parameter, external UV field) that determine the prevailing shock condition.

We use the recent shock model grid from Kristensen et al. (2023), based on the Paris-Durham code (Flower & Pineau des Fortés 2003; Godard et al. 2019), which computes the dynamical, thermal, and chemical structure of steady, plane-parallel shocks over $\sim 14,000$ models. The code determines pre-shock equilibrium conditions and includes self-consistent treatments of magnetic fields, UV irradiation, grain and PAH chemistry, and H_2 excitation and cooling. Depending on the shock speed and magnetic field strength, it solves for C , J , or C/J -type shocks. From each model, key outputs such as temperature, normalized upper state column density, H_2 integrated intensities, shock width, and molecular abundances are provided. Comparison of JWST observational H_2 data to the shock grid has been recently studied in other outflows (for e.g. see Le Gouellec 2025; Navarro et al. 2025), demonstrating the utility of the models in constraining shock properties.

The Kristensen et al. (2023) shock grid explores six key input parameters: the pre-shock density n_{H} ($10^2 - 10^8 \text{ cm}^{-3}$), the magnetic field scaling parameter b (0.1 – 10; where transverse magnetic field strength $B(\mu\text{G}) = b \sqrt{n_{\text{H}}}$), the shock velocity v_s ($2 - 90 \text{ km s}^{-1}$, dependent on b), the external UV field strength G_0 ($0 - 10^3$), the H_2 cosmic-ray ionization rate ζ_{H_2} ($10^{-17} - 10^{-15} \text{ s}^{-1}$), and the PAH abundance $X(\text{PAH})$ ($10^{-8} - 10^{-6}$). The parameters n_{H} , G_0 , ζ_{H_2} , and $X(\text{PAH})$ are sampled in factors of 10, while b and v_s vary non-uniformly.

We compared the observed extinction corrected upper state column densities from both outflows lobes (see Fig. B.3) to corresponding values predicted by the models. We did not restrict the initial conditions and explored the full parameter space. For each model, the reduced χ^2 was calculated to assess how well it reproduced the observed emission, and the model with min-

imum χ^2_{\min} was initially identified as the best fit. However, we found that several models can yield χ^2 values close to the minimum while having differing parameter values. To account for this degeneracy and obtain robust constraints on the likely physical conditions of the shock, we considered all models with $\chi^2 - \chi^2_{\min} < 10$. This value was chosen to provide a practical compromise by excluding clearly discrepant models while allowing exploration of the full parameter degeneracies in the model grid. The selection criteria resulted in 156 models that closely matched the observed emission. Fig. 10 shows the best and selected model fits on the observed data.

We next explored the properties of the selected models to evaluate the most common and statistically significant parameter values. Histogram analysis of the key different parameters are shown in Fig. 10. The analysis revealed that the majority of the selected models correspond to J -type shocks, indicating that these shocks are the dominant excitation mechanism in the observed regions. The magnetic field scaling factor b is low, with values between 0.1 and 0.3, consistent with the absence of strong C -type shock signatures. The shock velocities were found to be generally moderate, around 30 km s^{-1} , while the pre-shock densities range from $n_{\text{H}} = 10^4 - 10^5 \text{ cm}^{-3}$. The external UV radiation field G_0 was distributed mostly between 10 and 100, suggesting that UV irradiation contributes alongside collisional excitation. ζ_{H_2} and $X(\text{PAH})$ parameters are not considered much as the shock modeling has a very low dependence on them (Kristensen et al. 2023).

The significance of UV irradiation is highlighted in these results and suggests that, even if stellar UV is largely attenuated by the dense envelope, shock-generated UV can still be a substantial contributor to the shock structure, especially its tempera-

ture. At velocities ≥ 30 - 50 km s $^{-1}$, post-shock temperatures reach $\geq 10^5$ K, leading to H $_2$ dissociation and partial ionization. The hot post-shock gas then emits UV photons through both recombination and collisional excitation, creating a radiative precursor that enhances local photoionization. Recent study by [Navarro et al. \(2025\)](#) in HH 46 similarly found that *J*-shocks accompanied by a local UV field dominate the excitation of H $_2$. Therefore, moderate velocity dissociative *J*-shocks can provide a natural in situ UV source while collisionally exciting both the warm and hot H $_2$ components that dominate the observed emission. The relatively weak magnetic field further suppresses the formation of extended *C*-type shocks. Overall, our results indicate that moderate velocity *J*-type shocks, combined with a modest UV field, provide the best match to the observed H $_2$ emission in L1527.

5. Discussion

The JWST observations reveal a detailed hourglass-shaped bipolar outflow in the MIR broadband images (see Fig. 1). The images exhibit multiple nebulous features consisting of warm and hot layers of gas and dust generated within the outflow cavity. Our spectral maps reveal that the emission includes molecular, ionized and scattered light. In spite of such detailed composition, we do not see any trace of a large scale collimated jet in the broadband images. Such an absence of a large jet signature is distinctive and unique for L1527 given its evolutionary stage. In contrast, recent JWST observations of several other Class 0/I protostars like HH 211, HH 46, TMC 1, IRAS 16253-2429, have shown to have prominent jet emission. Their bulk of the emission is particularly traced in high-*J* H $_2$ and [Fe II] lines ([Ray et al. 2023](#); [Nisini et al. 2024](#); [Tychoniec et al. 2024](#); [Narang et al. 2024](#)). We see that most of L1527's dominant emission comes from the wide angle outflow across both molecular and ionized emission. However, the detection of double peaked ionized lines with the HV component having velocities ≥ 100 km s $^{-1}$ gives compelling evidence for the presence of a jet. This jet signature spans less than 500 au from the protostar and is fainter in relation to the jets from other sources. In addition, when compared to the large scale outflow structures (> 3000 au), the jet is small and covers only a fraction of the region, thereby concealing its visibility in the broadband images.

Double peaked emission lines with kinematics similar to L1527 have been observed in other protostellar outflows. For instance, HH 34 presents a collimated jet showing two velocity components both in molecular and ionized lines ([Nisini et al. 2016](#)). Using VLT observations of H $_2$ and [Fe II] lines, [Garcia Lopez et al. \(2008\)](#) showed that HH 34 LV component is distributed at ~ 15 - 50 km s $^{-1}$ surrounding a fast axial jet (~ 90 - 140 km s $^{-1}$). Likewise, in DG Tau, [Fe II] and [Ne III] double peaked lines were observed with VLT: SINFONI and X-shooter showing a similar velocity separation ([Agra-Amboage et al. 2011](#); [Liu et al. 2016](#)). Many other sources exhibit the same pattern, for e.g. SVS 13, HH 211, HH 46 ([Takami et al. 2006](#); [Tabone et al. 2017](#); [Garcia Lopez et al. 2010](#)). Such profiles are rarely seen in Class 0 protostars due to their dense envelopes, but more notable in Class II protostars due their moderate extinction. A unifying scenario in all these observations is that the LV component is associated to a slower wider wind, while the HV component traces the faster jet, thereby pointing to a stratified structure in the outflow.

The observed double peak lines can also be interpreted within the framework of shock models. The coexistence of the LV and HV components in the ionized lines suggests a stratified

velocity structure within predominantly *J*-type shock environment. Our comparison to models shows that moderate velocity (~ 30 km s $^{-1}$) *J*-type shocks illuminated by non-zero UV field best reproduce the observed emission. This suggests that the bulk of the line excitation is driven by compact, dissociative shock fronts likely associated to the disk wind. The high [Ne II]/[Ne III] ratio across most of the emitting region indicates soft ionization overall, consistent with moderate-velocity shocks where UV photons generated in the shock front contribute to the ionization. However, the clear detection of HV component in [Ar II], [Ne III] and [Fe II] specifically indicates a localized contribution from a faster jet. The HV component, particularly in [Ne III] is significant as ionization of Neon requires energies > 40 eV, typically only achieved via fast dissociative *J*-type shocks (> 80 km s $^{-1}$) ([Hollenbach & McKee 1989](#); [Shang et al. 2010](#)), as strong X-ray/UV photoionization is unlikely in L1527. The inferred jet velocity (> 100 km s $^{-1}$) in L1527 is consistent with predictions of a shock-excited jet emerging from the inner disk, suggesting the existence of a high-velocity jet core. All together, these observations support a stratified jet-outflow structure in which the fast jet core produces HV component in the ionized lines, while the moderate velocity *J*-type shock with intermediate UV field contributes to the broader LV component throughout the outflow.

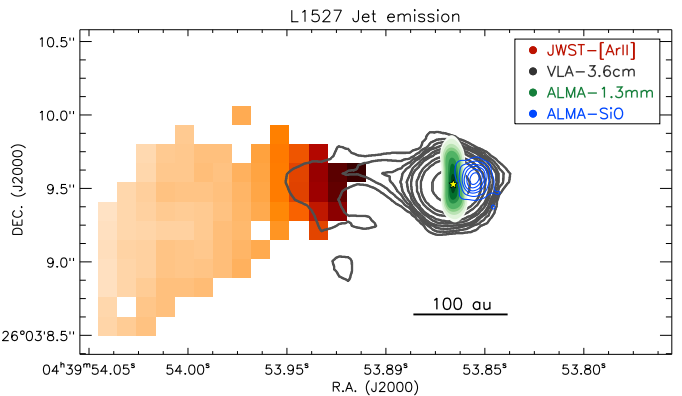


Fig. 11. The complete map of jet emission in L1527. Red colors show the JWST [Ar II] HV component jet emission. Black contours show the VLA 3.6 cm thermal emission ([Reipurth et al. 2004](#)). Green color show the ALMA 1.3 mm disk emission. Blue contours show the ALMA SiO jet emission ([van't Hoff et al. 2023](#)). Position of the central star is shown as a star symbol.

Radio observations have been used to detect jets based on the continuum emission arising from the thermal Bremsstrahlung radiation (free-free emission) (e.g. [Anglada et al. 1998](#); [Furuya et al. 2003](#)). An earlier study of L1527 by [Reipurth et al. \(2004\)](#) using VLA 'A' configuration at 3.6 cm observed an extended continuum jet in the eastern region close to the protostar. The jet emission was extended to about 150 au and was seen to curve towards the south on its leading end (see black contours in Fig. 11). This detection was not taken into consideration, as it was speculated that it may be due to a binary as proposed by [Loinard et al. \(2002\)](#). However, based on recent high-sensitivity observations it was shown that L1527 is not a binary (e.g. [Nakatani et al. 2020](#); [Sheehan et al. 2022](#)). Correlating the morphology of the radio jet to the MIRI jet, we find similarity in the distribution. The jet axis matches spatially extending towards the east and bending/curving towards the south. The curving of the jet could be due to wiggling/precession or an interaction with a dense layer of gas. A key feature that can be interpreted from both obser-

vations is the proper motion of the jet. The radio jet extends approximately to about 150 au, whereas the MIRI jet emission extends up to 500 au. There is a difference of about 350 au in length between both the emissions which have a time difference of 20 years. Based on this, a rough estimate of the average tangential velocity of the jet would lead to around 83 km s^{-1} . A main caveat in this estimate is that both data sets are observed at different wavelengths, therefore the difference in the jet length may also be associated to the emission from different layers of gas.

More recently, [van't Hoff et al. \(2023\)](#) carried out ALMA observations and detected a noticeable SiO emission on the western side (see blue contours in Fig. 11). SiO predominantly traces high density ejection material that are associated to jets in the innermost regions of Class 0/I protostars (e.g. HH 212; [Lee 2020](#)). The SiO emission observed in L1527 is compact and positioned very close to the protostar ($\sim 10\text{--}50$ au). Most importantly, it is blue shifted and exhibits higher velocity when compared to ALMA CO observations. When considered alongside our MIRI jet emission on the eastern side, this detection strongly supports the bipolar nature of jet in L1527. In addition their velocities and position confirm that the eastern region is red shifted while the western region is blue shifted consistent with the [Ne II] velocity maps (see Fig. 6). [van't Hoff et al. \(2023\)](#) also examined a large scale ^{12}CO map and found hints of a collimated CO emission on the western side at a distance of around 500–800 au. This emission was seen to be more resolved, flowing along the outflow axis, but had lower velocity than SiO emission. Therefore, it could not be confirmed as a large scale jet.

While the L1527 outflow exhibits a clear bipolar structure, the jet emission traced by HV component and SiO appear asymmetric and poorly distributed. The confinement of the HV component to one region may reflect the effects due to combination of inclination, asymmetries in the medium, or an episodic accretion. Asymmetric jets have been observed in other deeply embedded sources such as L1448-C ([Dionatos et al. 2009](#)), BHR 71 ([Gusdorf et al. 2015](#)), HH 46/47 ([Zhang et al. 2016](#)) and TMC 1 ([Tychoniec et al. 2024](#)), where external density gradients or variable accretion lead to predominantly one-sided jet activity. The inhomogeneity of the medium significantly changes the excitation conditions leading to emission in only certain tracers for each region. Many theoretical simulations lend strong support to this interpretation. For instance, [Raga et al. \(2002\)](#) modeled jets in young stars and showed how early-stage jets can produce compact, asymmetric jet features, particularly when interacting with clumpy or inhomogeneous envelopes. [Hansen et al. \(2016\)](#) conducted 3D MHD simulations of Class 0 jets and found that early jet interactions with over-dense clumps can produce complex asymmetric shock structures. In addition, such interactions also produce number of reverse shocks along the flow, which seems to be the case in L1527 (see Fig. 1). Moreover, it is believed that magnetic fields play a crucial role in shaping the jet structures ([Cerdeira & Gouveia Dal Pino 2001; Pudritz & Ray 2019](#)). Variations in magnetic field topology can lead to jets with uneven or asymmetric outflows. Different configurations of magnetic fields, such as misalignments between the field and the rotation axis due to warped disk, or non-uniform field structures, can result in one side of the jet being less collimated or more powerful than the other.

Another factor attributing to L1527 jets morphology is the evolutionary stage. While L1527 is classified as a Class 0/I transitional object, its jet appears unusually weak and compact. This indicates that the jet activity may have declined or it undergoes episodes of periodic mass-loss. Such temporal evolution has been seen in sources like L1448-C, IRAS 16293-2422, Ser-

pens South C7, where compact jets coexist with broader molecular flows, and signs of episodic accretion are common ([Bachiller et al. 1990; Kristensen et al. 2011; Plunkett et al. 2015](#)). Spitzer IRAC observations of L1527 taken 12 months apart show variability in total flux and variability in the emission in each outflow lobes ([Tobin et al. 2008](#)). Such variations are typically associated to asymmetric changes in accretion. The mass accretion rates inferred from modeling of L1527 show it to be $\dot{M}_{\text{acc}} \approx 3\text{--}7 \times 10^{-7} \text{ M}_\odot \text{yr}^{-1}$ ([Tobin et al. 2010; Flores-Rivera et al. 2021](#)). These values are two orders of magnitude higher when compared to values from Class II protostars, indicating that L1527 is still young. Recent JWST NIRSpec observational estimate on mass accretion rate show it to be $\dot{M}_{\text{acc}} \approx 1.0 \times 10^{-7} \text{ M}_\odot \text{yr}^{-1}$ and supports a non-steady and asymmetric accretion scenario in L1527 ([Drechsler et al. 2026](#)).

A key morphological characteristic of L1527 when compared to other Class 0/I protostars is the poor collimation of the outflow and jet emission. It is still unclear whether collimation of jet is a factor of age or environment. However, the common consensus is that as protostars evolve over time, the degree of collimation tends to decrease. This trend is also accompanied by a change in jet properties, such as transitioning from predominantly molecular emission to primarily ionized emission ([Frank et al. 2014; Bally 2016; Mottram et al. 2017](#)). In the case of L1527, we do not see any evidence of a molecular jet in the MIRI/MRS H₂ integrated intensity maps (see Fig. 3). Instead, most of the molecular emission is tracing the poorly collimated disk wind. We measured the outflow opening angle using the MIRI broadband images by tracing the cavity walls from about 2000 au down to less than than 50 au near the protostar. The estimated opening angle is about $84^\circ \pm 3$ considering no correction for inclination as the outflow is almost in the plane-of-sky. This is consistent with previous estimate of 85° by [Tobin et al. \(2008\)](#) using Spitzer IRAC images. [Dunham et al. \(2024\)](#) studied opening angles of 46 outflows in Perseus cloud and found that outflows widen during the Class 0 phase as they clear dense envelope material, but reach a 90° limit by Class I when most of the envelope has been dispersed and further expansion is no longer supported.

The unusually wide opening angle and lack of a well-collimated molecular jet makes L1527 a unique jet-launching system and suggests either an atypical evolution pathway or the combination of MHD processes and environmental conditions. In particular, magnetocentrifugal winds are thought to self-collimate due to stresses generated by magnetic field lines anchored in the disk or the disk-star interface ([Shu et al. 1994; Pudritz et al. 2007](#)). A strong poloidal magnetic field near the disk is responsible for the initial launch and collimation. As the flow propagates, the disk rotation twists the field lines, generating toroidal magnetic field that further collimates the outflow at larger distances ([Shang et al. 2006](#)). When the poloidal field near the disk is weak due to turbulence, envelope infall or disk misalignment, the initial outflow will be poorly collimated and subsequent buildup of toroidal fields may not be sufficient to produce strong collimation. Numerical simulations (e.g. [Tomisaka 1998; Hennebelle & Fromang 2008; Joos et al. 2012](#)) demonstrate that when the poloidal field strength is low or the field is strongly misaligned with the rotation axis, the resulting outflows are wide and poorly collimated.

[Segura-Cox et al. \(2015\)](#) carried out subarcsecond polarization observations of L1527 at 1.3 mm and found a dominant toroidal field in the region without any poloidal component. In addition, they found the magnetic field to be misaligned with the rotation axis. However, recent high sensitivity polarization

studies suggest that such polarized emission may primarily trace scattered light and not the intrinsic magnetic field structure (Harrison et al. 2021; Lin et al. 2024). Nevertheless, if taken as a direct tracer, this result combined with our observed morphology is consistent with a scenario of a weak misaligned poloidal field responsible for poor collimation. The strength of the magnetic field in the region also plays an important role in the degree of collimation. Several observations using dust polarization and Zeeman splitting have shown that Class 0/I protostars with highly collimated jets have magnetic field strengths in the order of 1-100 mG at scales less than 100 au, for e.g. IRAS 16293-2422, HH 211 and L1448 IRS2 (Alves et al. 2012; Lee et al. 2018; Kwon et al. 2019). In contrast, in protostars like IRAS 15398-3359 (Redaelli et al. 2019), where the outflows are less collimated, inferred field strengths at similar scales are lower, on the order of 10-100 μ G. So far there has not been any direct measurement of magnetic field strength in L1527. However, Davidson et al. (2014) tested different magnetic field models with observed polarization configurations to reproduce the observed disk and outflow morphology. They found that only the weakly aligned magnetic field model with strengths of about 100 μ G favors the observed morphology. Therefore, it is likely that the magnetic field in L1527 is weak and contributes to the poor collimation leading to broad, wide-angle flows rather than narrow jets. These properties in L1527 suggest that even in the earliest embedded stages, variation in magnetic field configuration, in addition to environmental conditions, strongly influence the collimation and shaping of the outflow structures.

6. Summary and Conclusions

We present JWST MIRI/MRS spectral observations towards a young low-mass Class 0/I protostar: L1527. This study has provided a detailed characterization of the physical and kinematic properties within the innermost 500 au region of the L1527 outflow. Through high-resolution spectroscopic observations we identified several molecular, atomic and ionized lines tracing distinct outflow components. The most striking result observed is the presence of a short and poorly collimated high velocity ionized jet in the eastern region, previously undetected, which highlights the accretion onto the protostar. Conversely, no molecular H₂ jet is detected in the MIRI data at smaller scales, nor a CO jet at larger scales in other studies, making L1527 outflow a unique flow among flows from young stars. Below, we summarize the main results of our study.

- Broadband MIR imaging of L1527 reveals a bright bipolar structure consisting of several filaments, bow shocks, knots and reverse shocks, dominated by scattered light. The outflow lobes are significantly bright and have a large opening angle of $84^\circ \pm 3$.

- The MIRI/MRS spectra reveal a chemically rich environment composed of molecular, atomic and ionized species. Pure rotational H₂ $\nu = (0-0)$ transitions from S(1) to S(8) are observed, with S(4) and S(5) being the strongest. The lines appear to be associated to a single component of the outflow, most likely the outflow cavity wall.

- Forbidden lines of [Ni II], [Ar II], [Ne II], [Ne III], [S I], and [Fe II], were detected tracing distinct ionized layers within the outflow. [Ar II], [Ne II], and [Fe II] show widespread shock excitation.

- [Ne II] channel maps highlight spatially distinct emission regions, indicating shock activity. The radial velocity map shows the eastern lobe is redshifted and the western lobe blueshifted, contrary to earlier interpretations. The average radial velocity

was found to be $\sim 30 \text{ km s}^{-1}$.

- Double peaked emission profiles in [Ar II], [Ne III], and [Fe II] lines were detected and found confined only to the eastern region. The LV ($\sim 30 \text{ km s}^{-1}$) component traces the material associated with the general disk wind, while the HV (100 km s^{-1}) component traces a poorly collimated fast jet extending up to ~ 500 au from the protostar.

- Excitation diagram analysis of H₂ rotational lines reveal two distinct gas layers: a warm component ($T_{\text{warm}} \approx 550 \text{ K}$, $N(\text{H}_2)_{\text{warm}} \approx 10^{20} \text{ cm}^{-2}$) and a hot component ($T_{\text{hot}} \approx 2500 \text{ K}$, $N(\text{H}_2)_{\text{hot}} \approx 10^{18} \text{ cm}^{-2}$). The spatial variations in temperature and column density maps closely follow the outflow morphology in H₂ emission, suggesting that gas heating and compression are strongly linked to a common excitation mechanism.

- Comparison of molecular and ionized emission with shock models indicate that moderate velocity *J*-shocks with modest UV field are the dominant driver for the widespread excitation of the observed lines.

Overall, the JWST MIRI/MRS observations of L1527 offers new insights into the early phases of protostellar evolution. The data reveal a chemically rich environment shaped by dynamic interactions and shocks. The outflow exhibits a stratified structure of molecular and ionized gas, where compact jet coexists with a slower wide-angle disk wind, that are likely driven by weak magnetic fields. These findings suggest that stratified wide angle outflows are active even in deeply embedded stages, challenging assumptions that such features are confined to later stages. Future high-spatial-resolution observations combined with magnetic field studies will be essential to further constrain the origin and dynamics of the outflow/jet structures.

Acknowledgements. This work is based on observations made with the NASA/ESA/CSA James Webb Space Telescope. The data were obtained from the Mikulski Archive for Space Telescopes at the Space Telescope Science Institute, which is operated by the Association of Universities for Research in Astronomy, Inc., under NASA contract NAS 5-03127 for JWST. These observations are associated with program PID 1290 and PID 1798. This research has been supported by the European Research Council advanced grant H2020-ER-2016-ADG-743029 under the European Unions Horizon 2020 Research and Innovation program. This paper makes use of the following ALMA data: ADS/JAO.ALMA 2019.1.00261.L and ADS/JAO.ALMA 2019.A.00034.S. ALMA is a partnership of ESO (representing its member states), NSF (USA) and NINS (Japan), together with NRC (Canada), MOST and ASIAA (Taiwan), and KASI (République of Korea), in cooperation with the Republic of Chile. The Joint ALMA Observatory is operated by ESO, AUI/NRAO and NAOJ. EvD, LT, LF and MvG acknowledge support from ERC Advanced grant 101019751 MOLDISK, TOP-1 grant 614.001.751 from the Dutch Research Council (NWO), the Netherlands Research School for Astronomy (NOVA), the Danish National Research Foundation through the Center of Excellence InterCat (DNRF150), and DFG grant 325594231, FOR 2634/2. A.C.G. acknowledges support from PRIN-MUR 2022 20228JPA3A The path to star and planet formation in the JWST era (PATH) funded by NextGeneration EU and by INAF-GOG 2022 NIR-dark Accretion Outbursts in Massive Young stellar objects (NAOMY) and Large Grant INAF 2022 YSOs Outflows, Disks and Accretion: towards a global framework for the evolution of planet forming systems (YODA). H.B. acknowledges support from the Deutsche Forschungsgemeinschaft in the Collaborative Research Center (SFB 881) The Milky Way System (subproject B1). P.J.K. acknowledges financial support from the Science Foundation Ireland/Irish Research Council Pathway programme under Grant Number 21/PATH-S/9360. The following National and International Funding Agencies funded and supported the MIRI development: NASA; ESA; Belgian Science Policy Office (BELSPO); Centre Nationale d'Etudes Spatiales (CNES); Danish National Space Centre; Deutsches Zentrum für Luft- und Raumfahrt (DLR); Enterprise Ireland; Ministerio De Economía y Competitividad; Netherlands Research School for Astronomy (NOVA); Netherlands Organisation for Scientific Research (NWO); Science and Technology Facilities Council; Swiss Space Office; Swedish National Space Agency; and UK Space Agency. The authors acknowledge the use of SAOImage DS9 software which is developed with the funding from the Chandra X-ray Science Center, the High Energy Astrophysics Science Archive Center and JWST Mission office at Space Telescope Science Institute.

References

Agra-Amboage, V., Dougados, C., Cabrit, S. and Reunanen, J., 2011, *A&A*, 532, A59

Alves, F. O., Vlemmings, W. T., Girart, J. M., & Torrelles, J. M. 2012, *A&A*, 542, A14

Anglada, G., Villuendas, E., Estalella, R., M. T., Beltran, M., et al. 1998, *AJ*, 116, 2953

Anglada G., Rodriguez, L. F., Carrasco-Gonzalez, C., 2018, *A&ARv*, 26, 3

Arce, H. G., Mardones, D., Corder, S., Garay, G., et al. 2013, *ApJ*, 774, 1

Argyriou, I., Glasse, A., Law, D. R., Labiano, A., et al. 2023, *A&A*, 675, A111

Aso, Y., Ohashi, N., Aikawa, Y., et al. 2017, *ApJ*, 849, 56

Bachiller, R., Cernicharo, J., Martin-Pintado, J., Tafalla, M., & Lazareff, B. 1990, *A&A*, 231, 174

Banerjee, R., Pudritz, R. E., 2006, *ApJ*, 641, 949

Banerjee, R., Pudritz, R. E., 2007, *ApJ*, 660, 479

Bally, J., 2016, *ARA&A*, 54, 491

Beuther, H., van Dishoeck, E., Tychoniec, L., Gieser, C., Kavanagh, P. J., et al. 2023, *A&A*, 673, A121

Blandford, R. D., Payne, D. G., 1982, *MNRAS*, 199, 883

Bitner, M. A., Richter, M. J., Lacy, J. H., et al. 2008, *ApJ*, 688, 1326

Beverly, Lynds, 1962, *ApJS*, 7, 1L

Bushouse, H., Eisenhamer, J., Nadia, D., Davies, J., et al. 2023, Zenodo, JWST calibration pipeline.

Bontemps, S., Andre, P., Terebey, S., Cabrit, S., 1996, *A&A*, 311, 858

Caratti o Garatti, A., Ray, T. P., Kavanagh, P., McCaughrean, M. J., et al. 2024, *A&A*, 691, A134

Cerdeira, A. H. & Gouveia Dal Pino, E. M., 2001, *ApJ*, 560, 779

Christiaens, V., Gonzalez, C., Farkas, R., et al. 2023, *J. Open Source Software*, 8, 4774

Crouzet, N., Mueller, M., Sargent, B., Lahuis, F., Kester, D., et al. 2025, *A&A*, 698, A77

Davidson, J., Li, Z.-Y., Hull, C., Plambeck, R., Kwon, W., Crutcher, R., et al. 2011, *ApJ*, 979, 74

Davis, C. J., Gell, R., Khanzadyan, T., Smith, M. D., Jenness, T. 2010, *A&A*, 511, A24

Davis, C. J., Cervantes, B., Nisini, B., Giannini, T., et al. 2011, *A&A*, 528, A3

Devaraj, R., Caratti o Garatti, A., Ray, T. P., Dewangan, L. K., et al. 2023, *ApJ*, 944, 226

Delabrosse, V., Dougados, C., Cabrit, S., Tabone, B., et al. 2024, *A&A*, 688, A173

Dionatos, O., Nisini, B., Garcia Lopez, R., Giannini, T., Davis, C. J., et al. 2009, *ApJ*, 692, 1

Drechsler, B., Tobin, J., Sheehan, P., Looney, L., et al. 2026, *ApJ*, Submitted

Dunham, M. M., Arce, H. G., Mardones, D., et al. 2014, *ApJ*, 783, 29

Dunham, M., Stephens, I., Myers, P., Bourke, T., Arce, H. G., et al. 2024, *MNRAS*, 533, 4

Eislöffel, J., Mundt, R., Ray, T. P., & Rodriguez, L. F. 2000, PPIV, Univ. of Arizona Press), 815

Frank, A., Ray, T. P., Cabrit, S., Hartigan, P., Arce, H. G., et al. 2014, PPVI, Univ. of Arizona Pres, 451

Federrath, C., 2015, *MNRAS*, 450, 4035

Ferreira, J., 1997, *A&A*, 319, 340

Flores-Rivera, L., Terebey, S., Willacy, K., Isella, A., et al. 2021, *ApJ*, 908, 108

Flower, D. R. & Pineau des Forêts, G., 2003, *MNRAS*, 343, 390

Flower, D. R., & Pineau des Forêts, G. 2015, *A&A*, 578, A63

Feeley-Johansson, A., Purser, S. J. D., Ray, T. P., et al. 2019, *ApJ*, 885, L7

Francis, L., van Dishoeck, E., Caratti o Garatti, A., van Gelder, M. L., Gieser, C., et al. 2025, *A&A*, 694, A174

Froebrich, D., Smith, M., & Eisloffel, J., 2003, *Astrophysics and Space Science*, 287, p217

Furuya R. S., Kitamura Y., Wootten A., Claussen M. J., Kawabe R., 2003, *ApJS*, 144, 71

Galli, P., Loinard, L., Bouy, H., Sarro, L., et al. 2019, *A&A*, 630, A137

Garcia, P. V., Cabrit, S., Ferreira, J., Binette, L., 2001, *A&A*, 377, 609

Garcia Lopez, R., Nisini, B., Giannini, T., Eisloffel, J., Bacciotti, F., et al. 2008, *A&A*, 487, 1019

Garcia Lopez, R., Nisini, B., Eisloffel, J., Giannini, T., Bacciotti, F., et al. 2010, *A&A*, 511, A5

Gardner, J. P., Mather, J. C., Abbott, R., Abell, J. S., et al. 2023, *PASP*, 135, 068001

Giannini, T., Nisini, B., Lorenzetti, D., 2001, *ApJ*, 555, 40

Giannini, T., Nisini, B., Caratti o Garatti, A., Lorenzetti, D., 2002, *ApJ*, 570, L33

Gieser, C., Beuther, H., van Dishoeck, E., Francis, L., van Gelder, M. L., et al. 2023, *A&A*, 679, A108

Godard, B., Pineau des Forêts, G., Lesaffre, P., et al. 2019, *A&A*, 622, A100

Gomez-Ruiz, A., Gusdorf, A., Leurini, S., Codella, C., et al. 2012, *A&A*, 542, L9

Güdel, M., Lahuis, F., Briggs, K. R., et al. 2010, *A&A*, 519, A113

Gusdorf, A., Riquelme, D., Anderl, S., Eisloffel, J., Codella, C., et al. 2015, *A&A*, 575, A98

Guszejnov, D., Grudic, M. Y., Offner, S. S. R., et al. 2022, *MNRAS*, 515, 4929

Hansen, E. C., Frank, A., Hartigan, P. & Lebedev, S. V., 2016, *ApJ*, 837, 143

Harrison, R., Looney, L., Stephens, I., Li, Z.-Y., Teague, R., et al. 2021, *ApJ*, 908, 141

Hartigan, P., Raymond, J., & Hartmann, L. 1987, *ApJ*, 316, 323

Hennebelle, P., & Fromang, S., 2008, *A&A*, 477, 9

Hsieh, C.-H., Arce, H., Li, Z.-Y., Dunham, M., et al. 2023, *ApJ*, 947, 25

Hogerheijde M. R., van Dishoeck E. F., Blake G. A., van Langevelde H. J., 1998, *ApJ*, 502, 315

Hollenbach, D., & McKee, C., 1989, *ApJ*, 342, 306

Hollenbach, D., & Gorti, U., 2009, *ApJ*, 703, 1203

Joos, M., Hennebelle, P., & Ciardi, A., 2012, *A&A*, 543, A128

Jørgensen, J., Bourke, T., Myers, P., Di Francesco, J., van Dishoeck, E., et al. 2007, *ApJ*, 659, 479

Karska, A., Kaufman, M. J., Kristensen, L. E., et al. 2018, *ApJS*, 235, 30

Kristensen, L. E., Klaassen, P., Mottram, J., Schmalzl, M., et al. 2013, *A&A*, 549, L6

Kristensen, L. E., van Dishoeck, E. F., Mottram, J. C., Karska, A., et al. 2017, *A&A*, 605, A93

Kristensen, L. E., Godard, B., Guillard, P., et al. 2023 *A&A*, 675, A86

Kwon, W., Stephens, I. W., Tobin, J. J., Looney, L. W., Li, Z.-Y., et al. 2019, *ApJ*, 879, 25

Law, D. D., Morrison, J. E., Argyriou, I., Patapis, P., et al. 2023, *AJ*, 166, 45

Lee, C.-F., Mundy, L. G., Stone, J., Ostriker, E., 2002, *ApJ*, 576, 294

Lee, C.-F., Hwang, H.-C., Ching, T.-C., Hirano, N., 2018, *Nature*, 9, 4636

Lee, C.-F. 2020, *A&A* 28, 1

Le Gouellec, V., Lew, B., Greene, T., Johnstone, D., et al., 2025, *ApJ*, 985, 225

Lin, Z.-Y. D., Li, Z.-Y., Stephens, I., Fernandez-Lopez, M., et al. 2024, *MNRAS*, 528, 843

Liu, C.-F., Shang, H., Herczeg, G. J., and Walter F. M., 2016, *ApJ*, 832, 153

Loinard, L., Rodriguez, L. F., DAlessio, P., Wilner, D. J., & Ho, P., 2002, *ApJ*, 581, L109

Luhman, K., 2018 *ApJ*, 156, 271

Mottram, J. C., van Dishoeck, E. F., Kristensen, L. E., Karska, A., et al. 2017, *A&A*, 600, A99

McClure, M. 2009, *ApJ*, 693, L81

Nakatani, R., Liu, H. B., Ohashi, S., et al. 2020, *ApJ*, 895, L2

Narang, M., Manoj, P., Tyagi, H., Watson, D., Megeath, T., et al. 2024, *ApJ*, 962, L16

Navarro, M. G., Nisini, B., Giannini, T., Kavanagh, P., et al. 2025, *ApJ*, 995, 199

Neufeld, D. A., Hollenbach, D. J., Kaufman, M. J., et al. 2007, *ApJ*, 664, 890

Neufeld, D. A., Nisini, B., Giannini, T., et al. 2009, *ApJ*, 706, 170

Nisini, B., Bacciotti, F., Giannini, T., Massi, F., et al. 2005, *A&A*, 441, 159

Nisini, B., Giannini, T., Antoniucci, S., Alcalá, J. M., et al. 2016, *A&A*, 595, A76

Nisini, B., Navarro, M. G., Giannini, T., Antoniucci, S., et al. 2024, *A&A*, 967, 168

Öberg, K. I., Boogert, A. C., Pontoppidan, K. M., van den Broek, S., et al. 2011, *ApJ*, 740, 109

Offner, S., Arce, H., 2014, *ApJ*, 784, 61

Ohashi, N., Hayashi, M., Ho, P., & Momose, M., 1997, *ApJ*, 475, 211

Ohashi, N., Tobin, J., Jorgensen, 2023, *ApJ*, 951, 8

Oya, Y., Sakai, N., Leefloch, B., Lopez-Sepulcre, A., et al. 2015, *ApJ*, 812, 59

Pascucci, I., & Sterzik, M. 2009, *ApJ*, 702, 724

Pascucci, I., Banzatti, A., Gorti, U., Fang, M., et al. 2020, *ApJ*, 903, 78

Pascucci, I., Cabrit, S., Edwards, S., et al. 2023, *PPVII*, ASPC Series, Vol.9, 534,

Plunkett, A., Arce, H., Mardones, D., van Dokkum, P., et al. 2015, *Nature*, 527, 70

Pontoppidan, K., Boogert, A., Fraser, J., van Dishoeck, E., Blake, G., et al. 2008, *ApJ*, 678, 1005

Pontoppidan, K., Evans, N., Bergner, J., & Yang, Y.-L., 2024, *Research notes of AAS*, 8, 68

Pudritz, R. E., Ouyed, R., Fendt, C., Brandenburg, A., 2007, *PPV*, Univ. of Arizona press

Pudritz, R. E., & Ray, T. P., 2019, *Frontiers in Astronomy*, Vol 6

Raga, A. C., Velazquez, P. F., Canto, J., Masciadri, E., 2002, *A&A*, 395, 647

Ray, T., Dougados, C., Bacciotti, F., Eislöffel, J., & Chrysostomou, A. 2007, *PPV*, Univ. of Arizona press

Ray, T.P. & Ferreira, J., 2021, *New Astronomy Reviews*, 93, 101615

Ray, T.P., McCaughrean, M.J., Caratti o Garatti, A., et al. 2023, *Nature*, 623, E3

Redaelli, E., Alves, F. O., Santos, F. P., and Caselli, P., 2019, *A&A*, 631, A154

Reipurth, B., Rodriguez, L., Anglada, G. & Bally, J., 2004, *AJ*, 127, 1736

Rieke, G., Wright, G., Boker, T., Bouwman, J., et al. 2015, *PASP*, 127, 584

Rocha, W. R. M., van Dishoeck, E., Ressler, M. R., van Gelder, M. L., Slavicinska, K., Brunken, N. G. C., et al. 2024, *A&A*, 683, A124

Segura-Cox, D., Looney, L., Stephens, I., Fernandez-Lopez, M., Kwon, W., et al. 2015, *ApJ*, 798, L2

Shang, H., Glassgold, A. E., Frank, Shu, Susana, L., 2002, *ApJ*, 564, 853

Shang, H., Allen, A., Li, Z.-Y., et al. 2006, *ApJ*, 649, 845

Shang, H., Li Z.-Y., Hirano N., 2007, *PPV*, Univ. of Arizona Press, 261

Shang, H., Glassgold A. E., Wei-Chieh, L., et al. 2010, *ApJ*, 714, 1733

Sheehan, P. D., Tobin, J. J., Li, Z.-Y., van't Hoff, M., et al. 2022, *ApJ*, 934, 95

Shu F., Najita J., Ostriker E., Wilkin F., Ruden S., Lizano S., 1994, *ApJ*, 429, 781

Shu F. H., Galli D., Lizano S., Glassgold A. E., Diamond P. H., 2007, *ApJ*, 665, 535

Slavicinska, K., Tychoniec, L., Gabriela Navarro, G., et al. 2025, *ApJ*, 986, L19

Sternberg, A., & Dalgarno, A., 2007, *ApJ*, 338, 197

Takami, M., Chrysostomou, A., Ray, T. P., Davis, C. J., et al. 2006, *ApJ*, 641, 357

Tabone, B., Cabrit, S., Bianchi, E., Ferreira, J., et al. 2017, *A&A*, 607, L6

Tamura, M., Ohashi, N., Hirano, N., Itoh, Y., et al. 1996, *AJ*, 112, 5

Tazaki, R., Menard, F., Duchene, G., Villenave, M., et al. 2025, *ApJ*, 980, 49

Tobin, J. J., Hartmann, L., Calvet, N., D'Alessio, P., 2008, *ApJ*, 679, 1364

Tobin, J. J., Hartmann, L., Loinard, L., 2010, *ApJ*, 722, L12

Tobin, J. J., Hartmann, L., Chiang, H-F., Looney, L., 2011, *ApJ*, 740, 45

Tobin, J. J., Hartmann, L., Chiang, H-F., Wilner, D., 2012, *Nature*, 679, 1364

Tobin, J. J., Hartmann, L., Chiang, H-F., Wilner, D., 2013, *ApJ*, 771, 48

Tomisaka, K., 1998, *ApJ*, 502, L163

Towner, A. M., Ginsburg, A., DellOva, P., Gusdorf, A., et al. 2023, *ApJ*, 960, 48

Tychoniec, L., van Gelder, M. L., van Dishoeck, E., Francis, L., Rocha, W., et al. 2024, *A&A*, 687, A36

van Dishoeck, E., Tychoniec, L., Rocha, W., Slavicinska, K., Francis, L., et al. 2025, *A&A*, 699, A361

van Gelder, M. L., Francis, L., van Dishoeck, E., Tychoniec, L., Ray, T. P., et al. 2024, *A&A*, 692, A197

van't Hoff, M. L. R., Tobin, J. J., Li, Z.-Y., et al. 2023, *ApJ*, 951, 10

Wright, G., Rieke, G., Glasse, A., Ressler, M., Garcia Marin, M., et al. 2023, *PASP*, 135, 048003

Wu Y., Wei Y., Zhao M., Shi Y., et al. 2004, *A&A*, 426, 503

Yang, Y.-L., Green, J. D., Pontoppidan, K. M., et al. 2022, *ApJ*, 941, L13

Yildiz, U. A., Kristensen, L. E., van Dishoeck, E. F., et al. 2015, *A&A*, 576, A109

Zhang, Y., Arce, H. G., Mardones, D., et al. 2016, *ApJ*, 832, 158

Zhou, S., Evans, N. & Wang, Y., 1996, *ApJ*, 466, 296

Appendix A: MIRI/MRS spectral lines in the L1527 outflow.

Table A.1 and A.2 summarizes the list of detected molecular, atomic and ionized lines in the L1527 outflow with line intensities obtained at aperture positions in the eastern and western lobes.

Table A.1. Properties of the list of detected molecular H₂ pure rotational lines.

Molecular Line	Wavelength λ (μm)	Excitation Energy E_u/k_B (K)	Statistical Weight g_u	MIRI Channel-Grating	Line Intensity ($\text{W m}^{-2} \text{arcsec}^{-2}$) EAST	Line Intensity ($\text{W m}^{-2} \text{arcsec}^{-2}$) WEST
H ₂ (0-0) S(8)	5.05312	8677	21	ch1-SHORT	1.57×10^{-20}	2.11×10^{-20}
H ₂ (0-0) S(7)	5.51116	7197	57	ch1-MEDIUM	5.08×10^{-19}	4.07×10^{-19}
H ₂ (0-0) S(6)	6.10856	5830	17	ch1-MEDIUM	5.45×10^{-20}	4.87×10^{-20}
H ₂ (0-0) S(5)	6.90952	4586	45	ch1-LONG	7.61×10^{-19}	6.57×10^{-19}
H ₂ (0-0) S(4)	8.02505	3474	13	ch2-SHORT	7.08×10^{-19}	6.82×10^{-19}
H ₂ (0-0) S(3)	9.66491	2504	33	ch2-MEDIUM	5.39×10^{-20}	4.23×10^{-20}
H ₂ (0-0) S(2)	12.2786	1682	9	ch3-SHORT	4.01×10^{-20}	4.72×10^{-20}
H ₂ (0-0) S(1)	17.0348	1015	21	ch3-LONG	7.83×10^{-20}	8.05×10^{-20}

Table A.2. Properties of the list of detected atomic and ionized lines.

Ion	Wavelength λ (μm)	Excitation Energy E_u/k_B (K)	Ionization Potential (eV)	Line ID	MIRI Channel-Grating	Line Intensity ($\text{W m}^{-2} \text{arcsec}^{-2}$) EAST	Line Intensity ($\text{W m}^{-2} \text{arcsec}^{-2}$) WEST
[Fe II]	5.341	2694	7.90	a ⁴ F _{9/2} -a ⁶ D _{9/2}	ch1-SHORT	3.84×10^{-19}	0.94×10^{-19}
[Ni II]	6.636	2168	7.64	² D _{3/2} - ² D _{5/2}	ch1-LONG	–	2.43×10^{-20}
[Ar II]	6.985	2060	15.76	² P _{1/2} - ² P _{3/2}	ch1-LONG	8.94×10^{-19}	–
[Ne II]	12.813	1123	21.56	² P _{1/2} - ² P _{3/2}	ch3-SHORT	3.17×10^{-18}	2.51×10^{-19}
[Ne III]	15.555	925	40.96	³ P ₂ - ³ P ₁	ch3-SHORT	3.75×10^{-19}	1.13×10^{-19}
[Fe II]	17.936	3497	7.90	a ⁴ F _{7/2} -a ⁴ F _{9/2}	ch3-LONG	2.06×10^{-19}	9.86×10^{-20}
[S I]	25.249	570	0	³ P ₁ - ³ P ₂	ch4-LONG	4.51×10^{-20}	6.28×10^{-19}
[Fe II]	25.988	554	7.90	a ⁶ D _{7/2} -a ⁶ D _{9/2}	ch4-LONG	1.93×10^{-20}	2.25×10^{-20}

Notes. Blank entries in the East and West line intensity columns indicate non-detection or intensity levels below the noise threshold.

Appendix B: Excitation diagram analysis

Figures B.1 and B.3 show the excitation diagram analysis results with the extinction corrected H_2 line intensities and two-component fits for observed values at aperture positions in the eastern and western lobes of L1527 outflow.

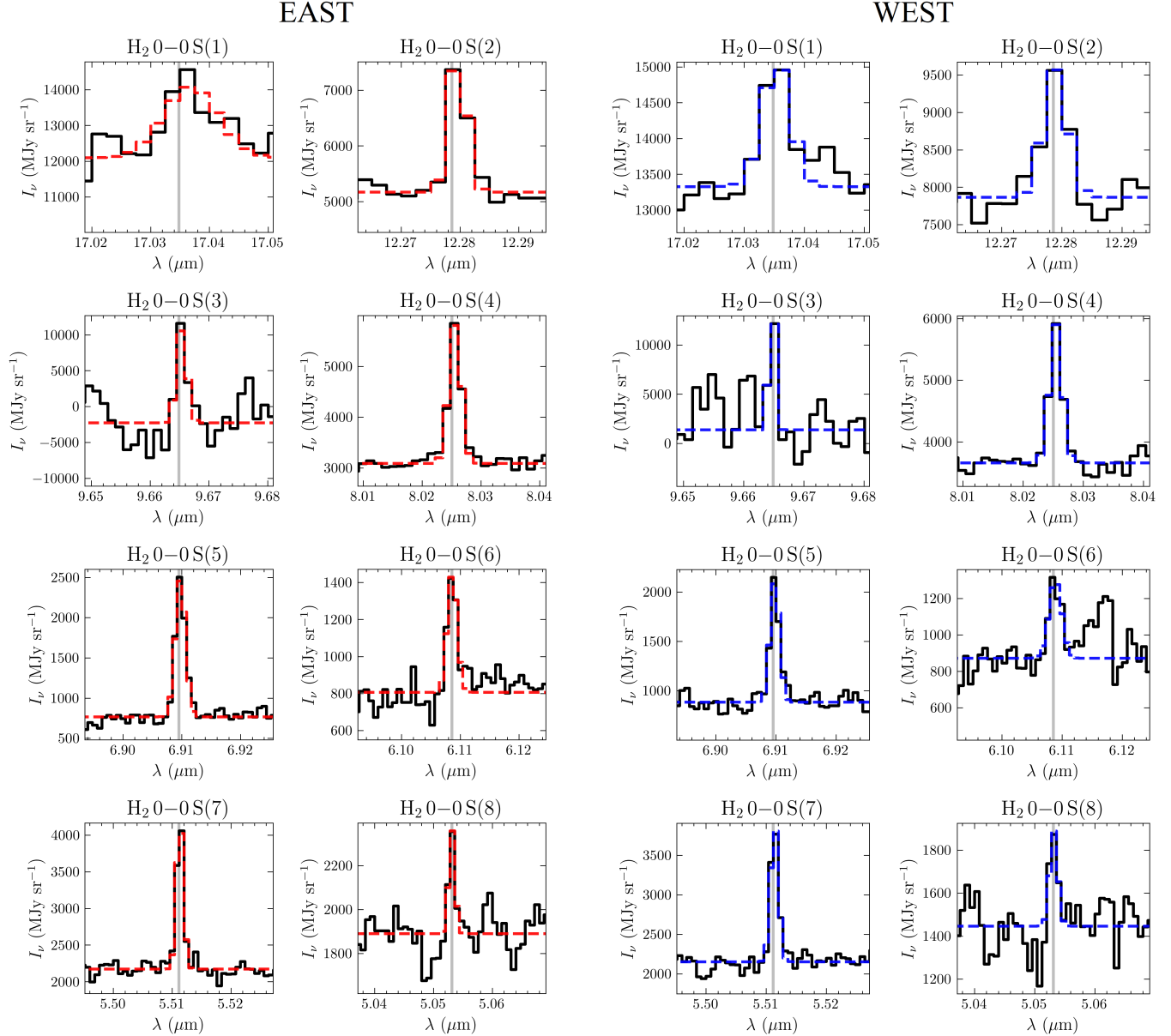


Fig. B.1. Extinction-corrected H_2 rotational lines from S(1) to S(8) transitions for example spaxels at aperture positions in the eastern and western lobes (see Fig. 1). The Gaussian fits to the lines are color-coded red and blue respectively for each region. The vertical grey line indicates the central wavelength of each transition.

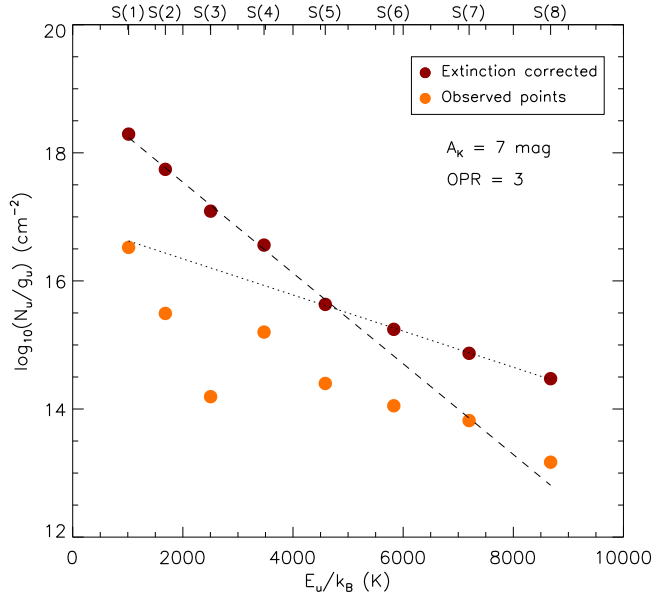


Fig. B.2. H₂ excitation diagram before and after extinction correction for transitions from S(1) to S(8) obtained at aperture position in the eastern lobe. Extinction correction of $A_K=7$ mag best represents the two component fit.

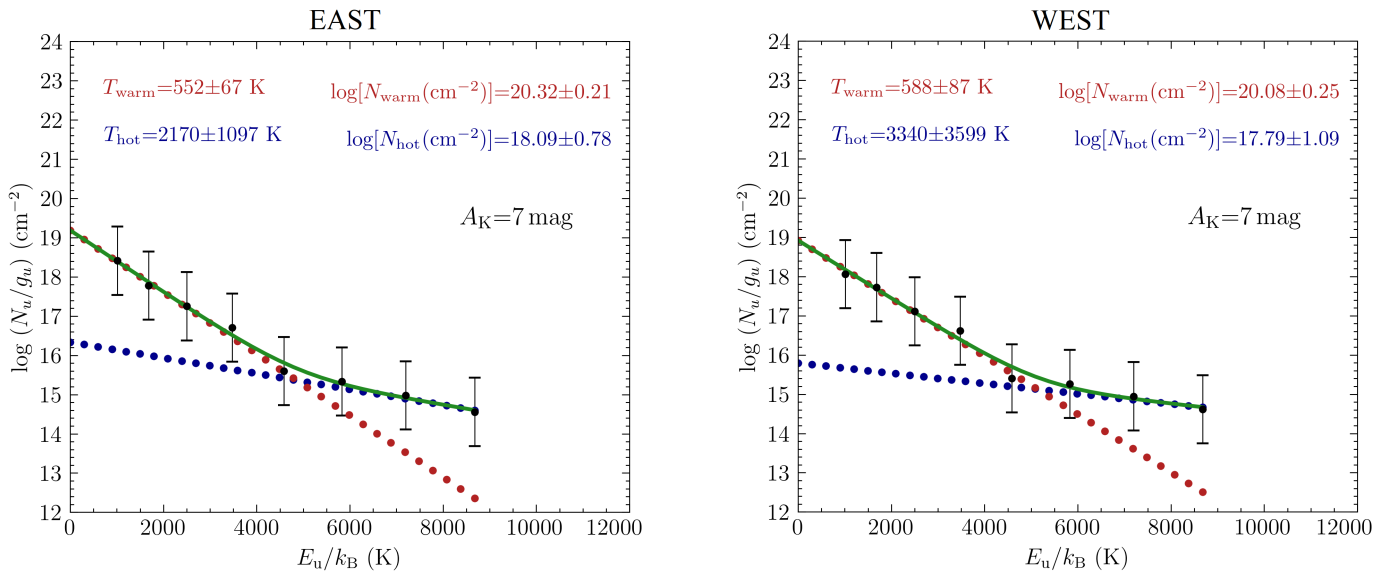


Fig. B.3. H₂ excitation diagram analysis with pdrtypy for the example spaxels at aperture positions in the eastern and western lobes (see Fig. 1). The extinction corrected line intensities converted to upper state column densities are shown as black data points with error bars. The two component fit to the data points is shown by red and blue dots, corresponding to the warm and hot component. The total fit is indicated by a green line. Values of estimated temperature and column density are shown at the top. The errors bars are estimated from uncertainties of the line integrated intensities and taking into account uncertainties in the absolute flux calibration (5%) and uncertainty in extinction (2 mag). These uncertainties are then propagated to the upper state column densities.